

Geochemistry and mineral chemistry of the armoor granitoids, eastern dharwar craton: implications for the redox conditions and tectono-magmatic environment

A. Ajay Kumar¹ · Ch. Ashok²

Received: 9 March 2023 / Revised: 23 September 2023 / Accepted: 11 October 2023 / Published online: 2 November 2023
© The Author(s), under exclusive licence to Science Press and Institute of Geochemistry, CAS and Springer-Verlag GmbH Germany, part of Springer Nature 2023

Abstract The mineralogical and geochemical characteristics of the K-rich granites from the Armoor granitic rocks in the northeastern portion of the Eastern Dharwar Craton (EDC) are presented. In order to understand its physico-chemical conditions, the petrogenesis of the granitoid was explained from biotite chemistry and geochemical systematics. Studies of mineral chemistry expose that compositionally, K-feldspar and plagioclase in Armoor granite rocks range from An₀, Ab_{3–5.9}, Or_{94–96.9} and An_{5–29}, Ab_{71.9–94.9}, Or_{0–1.5}, respectively. The mineral chemistry of biotite crystals exhibits composition that varies from primary to re-equilibrated primary biotites. Although biotites from the Armoor granites generally exhibit an I-type trend, with calc-alkaline parental magma in a subduction setting. Biotite chemistry of granites displays magnetite (oxidized) series nature, which has oxygen fugacity ($f\text{O}_2$) = – 15.1 to – 16.7(\log_{10} bar), under high oxidizing conditions. Temperature and pressure estimates for the crystallization of Armoor granites based on biotite composition are T = 612–716 °C and 1.0–0.4 kbar, respectively. Geochemically, these rocks are metaluminous to slightly peraluminous and magnesian, with calc-alkaline potassium-rich granite. On the chondrite normalized REE diagram, the granites have positive europium anomalies; rich Sr/Y, (Dy/Yb)_N ratios and reduced Mg[#], Rb/Sr, Rb, Sr indicate that the melting of earlier rocks, crystal accumulation and

residual garnet source formed at high pressures. The examined granites show that they are produced from the melting of crustal sources. Thus, the extensive analyses of the described Armoor granite suggest that they were produced by crust sources and developed under oxidizing conditions in subduction setting.

Keywords Armoor granites · Oxygen fugacity · Crystal accumulation · Remelting · Subduction

1 Introduction

The Neoarchean crust of the Eastern Dharwar Craton (EDC) consisted primarily of granitoids with diverse mineralogical, geochemical, and source characteristics (Dey et al. 2017; Jayananda et al. 2018, 2020; Mohan et al. 2019; Bhaskar Rao et al. 2020). In the northern section of EDC, researchers have given significance to studying the origin and evolution of granitoids from field, petrography, geochemistry and geochronological aspects (Dey et al. 2009, 2017; Jayananda et al. 2018, 2019, 2020; Mohan et al. 2019; Bhaskar Rao et al. 2020; Ajay Kumar et al. 2022; Nagamma et al. 2023). However, Mineralogical and Redox conditions studies are limited in the northern section of EDC (Ashok et al. 2022a; Raju et al. 2022). These studies provided valuable insight into the petrogenesis, physical and chemical environments of granites in connection with oxygen fugacity, temperature, and pressure (Kumar and Pathak 2010a; Bora and Kumar 2015; Anets-sungla et al. 2018; Babazadeh et al. 2019; Azadbakht et al. 2020; Sun et al. 2020).

The northern section of the EDC in southern India is composed of granitoids comprising granite gneiss, tonalite-

✉ Ch. Ashok
ashokchngri@gmail.com

¹ Department of Geology, Osmania University,
Hyderabad 500007, India

² CSIR-National Geophysical Research Institute,
Uppal, Hyderabad 500007, India

trondhjemite-granodiorite (TTG), and syeno-monzogranites, together with their corresponding mafic microgranular enclaves (MMEs) (Prabhakar et al. 2009; Ashok et al. 2022a, b; Raju et al. 2022). The age of these basement TTG rocks corresponds to the middle to late Archean and is represented by (Chadwick et al. 2000), subsequent by Archean to Proterozoic granitic events characterized by Closepet granite (Jayananda et al. 1995). Due to differing scholarly opinions, the origin of these granitoids remains a topic of debate. These granitoid magmas are mostly linked with collisional or subduction rifting, intraplate, and oceanic settings (Manikyamba and Kerrich 2012; Moyen et al. 2017; Jayananda et al. 2018, 2020).

The compositions and assemblages of common minerals in igneous rocks act as important tools that give crucial information about the magma's origin, the varying physicochemical state of melt during crystallization, and the resulting rock's post-solidus changes (Helmy et al. 2004; Kocak et al. 2011; Anettsungla et al. 2018; Azadbakht et al. 2020; Sun et al. 2020; Ashok et al. 2022a; Raju et al. 2022). To quantify the emplacement temperature (T) and pressure (P) of calc-alkaline igneous rocks, the thermobarometry of amphibole and biotite has been frequently utilized (Anderson and Smith 1995; Ridolfi et al. 2010). Biotite, which is a ferromagnesian mineral, occurs in most felsic igneous rocks and can resist different temperature and pressure conditions (Yavuz 2003). The parent melt's bulk composition largely determines mica composition and eventually re-equilibrates with the final volatile phase (Anettsungla et al. 2018; Babazadeh et al. 2019; Azadbakht et al. 2020; Khosravi et al. 2021). Therefore, biotite compositions may be utilized to detect various physicochemical properties of parent intrusions, viz., under the particular environment, it is developed (Speer et al. 1981; Tischendorf et al. 2001), thus, chemistry of biotite is important in terms of investigating hydrothermal and magmatic progress (Cotten 1979), and the granitic rocks petrogenesis (Machev et al. 2004; Kumar and Pathak 2010b; Y et al. 2015; Sheykhi et al. 2019). Moreover, the $\text{Fe}^{3+}/\text{Fe}^{2+}$ of biotite may be utilized to examine the host magma's oxygen fugacity (Wones and Eguster 1965; Wen et al. 2017; Khosravi et al. 2021). Also, the composition of biotite can be used to evaluate the equilibrium by analyzing the sub-solidus recrystallization or exchange processes amount within pairs and/or with some other minerals like potassium feldspar (Beswick 1973; Cotten 1979) and apatite (Wones 1980; Zhu and Sverjensky 1992; Sallet 2000). Felsic magmas, on the other hand, may be reduced or oxidized as a result of their interaction with pelitic country rocks and/or later tectonism initiated on the rocks (Cesare et al. 2008; Singh and Kumar 2008; Kumar et al. 2017). Many earlier research studies have established that biotite composition usage is a good reference to granite

petrogenesis as well as tectono-magmatic setting (Singh and Kumar 2005; Kumar and Pathak 2010a; Anettsungla et al. 2018; Babazadeh et al. 2019; Azadbakht et al. 2020; Khosravi et al. 2021; Ashok et al. 2022a). Furthermore, the traditional experimental studies show firmly developed the biotite is a reliable indication of granitic magma redox conditions (Wones and Eguster 1965; Wones 1972). The biotite composition may also be employed in certain situations as a tectono-magmatic indication (Abdel-rahman 1994; Nachit et al. 2005). In this paper, the research discusses the mineral compositions acquired by electron microprobe analysis (EMPA) and major and trace elemental data of Armoor granitoid, with the following objectives are (i) to explain the mineral-chemical development of the Armoor granite, (ii) to determine the physicochemical settings (crystallization temperature and pressure, and oxygen fugacity) that prevailed in the crystallization of the magma, and (iii) provide clues to their petrogenesis and role of crystal accumulation, hydrothermal alteration and geotectonic evolution in the Armoor granites.

2 Geological setting

The Dharwar Craton (DC) in southern India (Fig. 1a) corresponds to a massive oblique section of the Archaean continental crust with a long crustal history extending from 3.6–2.5 Ga and is a significant wide hot orogeny toward the end of the Neoarchean period (Chardon et al. 2011). This craton contains large regions of polyphase TTG gneisses locally recognized as peninsular gneisses, two generations of volcanic-sedimentary greenstone phases (younger Dharwar Super Group and older Sargur Group), SHRIMP U-Pb zircon ages as 2.62 and 3.0 Ga (Manikyamba and Kerrich 2012; Hokada et al. 2013; Jayananda et al. 2013; Dey et al. 2015, 2018; Manikyamba et al. 2015; Khanna et al. 2016) and calc-alkaline 2.57 to 2.50 Ga to High-K granitoid plutons (Jayananda et al. 2018, 2019, 2020; Mohan et al. 2019). It is divided into two crustal blocks such as the EDC and Western Dharwar Craton (WDC), based on the metamorphic patterns, structures, TTG-greenstones-granites abundance, and crustal thickness (Chadwick et al. 2000; Jayananda et al. 2006, 2020; Chardon et al. 2008, 2011). The steep mylonitic shear region along with the eastern limit of the Chitradurga belt, is identified as the separation line between the two crustal blocks (Chadwick et al. 2000; Chardon et al. 2008).

The Dharwar craton preserves Paleoarchean to Neoarchean magmatism connected with crust formation and reworking, which largely evolved to the development of the continental crust (Chadwick et al. 2000; Jayananda et al. 2018; Bhaskar Rao et al. 2020; Nagamma

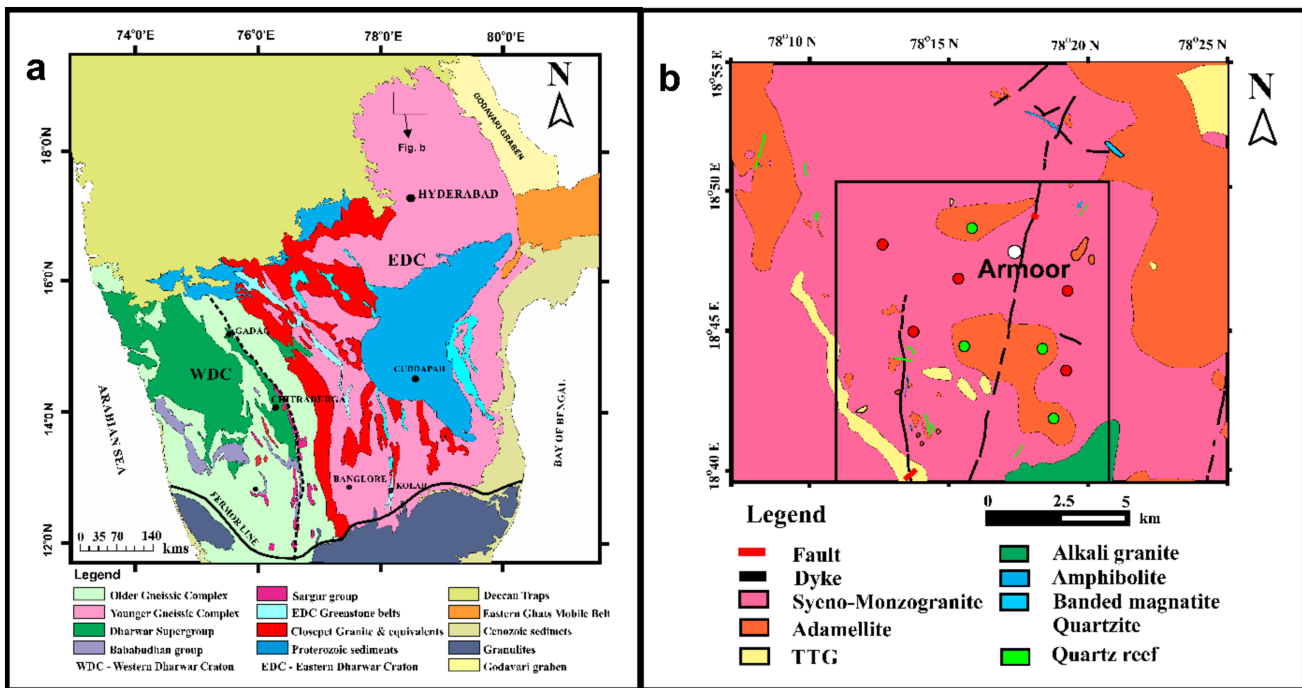


Fig. 1 **a** Geological map of the Dharwar craton (modified after Nagamma et al. (2022)). **b** Geological map of the Armoor granites showing the exposures of granitoids

et al. 2023). The Archaean basement within EDC is predominantly made up of 2.7 Ga tonalitic to granodioritic gneisses, with substantial remnants of 3.0 to 3.38 Ga TTG with greenstones Sargur-type with interlayers (mostly occurring as discontinuous 4–6 km long bands confined to the EDC's southwestern portion), volcanic-dominated greenstone belts ranging from 2.7 to 2.54 Ga, and the most voluminous N-S trending calc-alkaline plutonic belts ranging from 2.57 to 2.52 Ga (Friend and Nutman 1991; Nutman et al. 1996; Balakrishnan et al. 1999; Chadwick et al. 2000; Jayananda et al. 2000; Chardon et al. 2008; Dey et al. 2012; Gireesh et al. 2012). At 2.52 Ga, the basement TTG initiated reworking, which was connected to significant juvenile magmatic accretion and widespread shear deformation (Jayananda et al. 1995, 2000, 2018; Krogstad et al. 1995; Bhaskar Rao et al. 2020). High-T metamorphism and low-pressure impact the EDC, with conserved assemblies correlating to a dynamic transition from amphibolite into granulite facies dated at ca. 2.5 Ga (Peucat et al. 1993; Chadwick et al. 2000; Chardon et al. 2008; Jayananda et al. 2013). The Archaean Granitic Complex of the study region Nizamabad contains huge expanses of the territory comprised of various granitic intrusions. The Armoor Area constitutes a part of the Nizamabad District in Telangana State and is dominated by granites emplaced in a basement of TTG (Fig. 1b). The State Capital Hyderabad is roughly 181 miles southeast, and the district headquarters, Nizamabad, is about 27 km

from the study area. The study area under investigation is spread over about 110 km^2 with an oblate outline. Compositionally, the Armoor granite exhibits grey granite to pink granite; it shows syenogranite to monzogranite (Fig. 2a and b). Pink granite is pinkish to whitish grey color, whereas grey granite is whitish grey to grey color. These show sharp contact with hosted mafic magmatic enclaves and TTGs. Both granitic types consist of feldspar phenocryst and many late magmatic injections such as quartz veins, pegmatite veins, and other fluid interactions noticed in the study area. The mafic magmatic enclaves have interacted with host granites governing to magma mixing and mingling, which limited study in the northern part of EDC (Shukla and Mohan 2019; Ashok et al. 2022b; Raju et al. 2022).

3 Analytical procedures

The thin rock section was made and obtained petrographic characteristics at the Department of Geology, Osmania University, Hyderabad. The chemical analysis of feldspars and biotites from granite samples was performed on a carbon-coated polished portion with CAMECA SX 100 EPMA (Electron Probe Micro Analyzer) at the Geological Survey of India, Hyderabad. To accelerating voltage and beam current, the Faraday cup was set at 15 kV & 12 nA. A beam diameter of 5 μm was retained for the analysis of

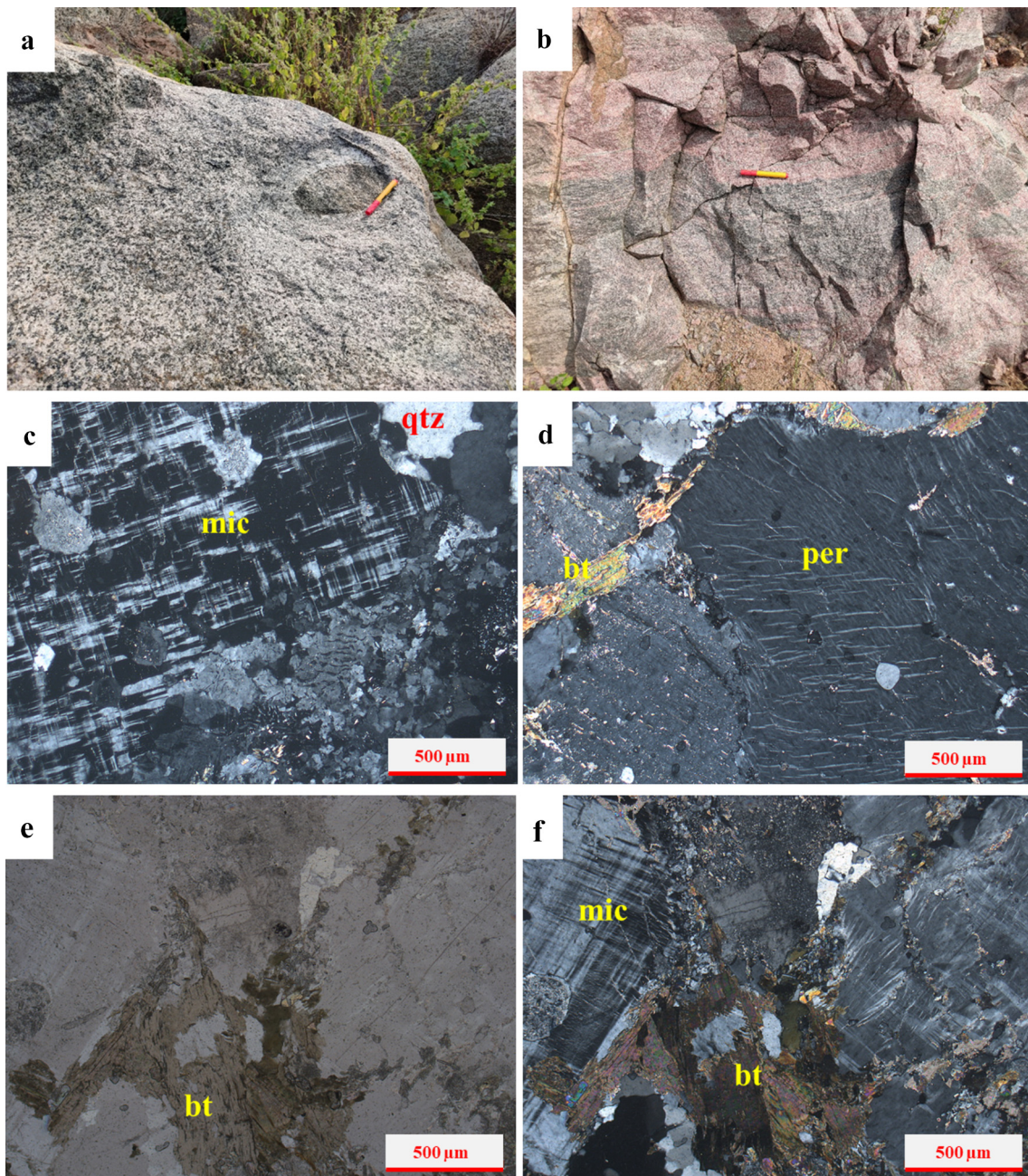


Fig. 2 **a** Sub-rounded enclave hosted in medium-grained grey granite. **b** Sharp contact between enclave and pink granite. **c** Microcline is displaying crosshatched texture associated with quartz grains. **d** Large perthite texture observed in grey granite with altered biotite. **e** Laths of biotite crystals (PPL), **f** XPL

biotite. Natural and synthetic minerals were utilized as standards for calibration given by CAMECA. After repeated assessments of relevant standards, it was discovered that the inaccuracy of the major elements was less than 1%. Ferrous iron is the term used to describe total iron.

Granite samples were crushed and powdered using an agate mill and a 200-mesh pulverizer. The X-Ray Fluorescence Spectrometer (XRF) at the CSIR-National Geo-physical Research Institute (CSIR-NGRI), was used to

determine the major element concentrations of pressed pellets with a relative standard deviation of 3%; the analytical method is described by (Krishna et al. 2007). Using the closed digestion process, materials were dissolved for trace element analysis. In 10 mL Saville containers containing a 7:3 HF:HNO₃ acid combination, 50 mg of representative sample powders were dissolved for 48 h at 150 °C in a 7:3 HF:HNO₃ acid mixture. After digestion, two to three drops of perchloric acid (HClO₄) were added to the

mixture, which was then evaporated until dry. Combine 20 mL of freshly prepared 1:1 HNO₃ and keep it at 80 °C for 10–15 min. After getting a clear solution, 5 mL of Rh (1 ppm concentration) was added as an internal standard, and then 250 mL was produced. This solution was diluted to the correct TDS content by adding 5–50 mL of water (total dissolved solids). Geological Survey of Japan-approved reference materials (JG-2 and JG-1) were used as standards for the examination of major and trace elements. The reference materials used to determine the accuracy and repeatability of the majority of trace components have an RSD of 5%.

4 Petrography

In the study area, pink and grey granites are distinguished by medium to coarse, equigranular to porphyritic, and hypidiomorphic textures. These granites consist chiefly of quartz, plagioclase (albite-oligoclase), K-feldspar (orthoclase and microcline), and biotite, along with the zircon, magnetite and sphene as accessory phases. Pink granite has a larger concentration of K-feldspar than plagioclase feldspar, whereas grey granite has a higher concentration of plagioclase than K-feldspar. Microcline with cross-hatched twinning characterizes K-feldspar, which is medium, subhedral to anhedral (interstitial) (Fig. 2c). Exsolution as well as intergrowth textures such as granophyres and perthite (Fig. 2d), are particularly widespread. The study area consists most prevalent ferromagnesian mineral is biotite. The biotite grains in Armoor's granite are greenish-brown (Fig. 2e and f), implying oxidized I-type intrusions as a host (Lalonde and Bernard 1993) (Fig. 5a). These subhedral to euhedral grains are relatively large and exhibit little alteration to chlorite (Fig. 2f), and include ilmenite, apatite, magnetite, and zircon as inclusion minerals. At spots, biotite poikilitically encloses zircon, magnetite, and titanite with pleochroic haloes and is seldom converted to chlorite (Fig. 2e and f).

The granites have dominantly observed crosshatched twining microcline and hosted plagioclase and quartz crystals, which might influence deformation (Fig. 3a). The microstructure of perthite is characterized by the intergrowth of alkali feldspar and plagioclase and surrounded by undulose quartz, which indicates to deformation (Ashok et al. 2021; Nagamma and Ashok 2022) (Fig. 3b). Plagioclase was strongly sericitized and featured twinned albite polysynthetic structures (Fig. 3c). Rarely, alkali feldspar exhibits sericite alteration (Fig. 3d). Sericitization indicates that the process of alteration has reached low temperatures. Biotite often appears as distinct laths or

aggregates transformed into chlorite and epidote. This unaltered plagioclase (Ab_{71.9–75.0}) exhibits oligoclase composition, whereas altered and mixed plagioclase (Ab_{92.0–95.0}) falls in the albite field of the Or-Ab-An diagram (Fig. 5a).

The mineral growth textures are observable under polarized microscopy. Furthermore, backscattered electron (BSE) images have been widely used in investigating mineral morphological structures, focusing on their chemical variability. In this work, the examination revealed the presence of micropores, microcracks, and textures associated with magmatic and post-magmatic crystallization in feldspar and biotite (Fig. 4). These crystals were euhedral to subhedral texture and porous nature. Alkali feldspar consists of porous plagioclase, albite-rich plagioclase (Fig. 4a). The plagioclase feldspar contains tiny alkali feldspar and biotite crystals and seritization (Fig. 4a). Large plagioclase patch inserted into alkali feldspar with small inclusions (Fig. 4b). Mixed of alkali feldspar and plagioclase feldspar produced albite-rich plagioclase (Fig. 4d). Biotite poikilitically enclosed plagioclase and associated Fe-Ti oxides (Fig. 4c and d). Plagioclase and biotite are coupled with large Fe-Ti oxides (Fig. 4a and d). Chlorite flakes are generally associated with biotite, which is alteration product (Fig. 4d).

5 Results

5.1 Mineral chemistry

5.1.1 Feldspar

Armoor granites were represented by 7 alkali feldspar compositions that were analyzed on the basis of 8 oxygen per atom (Table 1). Orthoclase dominates the composition of alkali feldspar in examined granites (Fig. 5a). Or_{94.0} to Or_{96.9} and Ab_{3.0} to Ab_{5.9}, are the compositions of alkali feldspar in the studied region. The most prevalent mineral in the examined rocks is a plagioclase feldspar. Table 2 lists typical plagioclase analyses and mole percentages (mol%) of anorthite, albite, and orthoclase calculated on eight oxygen per atom bases from 15 plagioclase spot analyses performed on Armoor samples. Plagioclase composition of the Armoor granite ranges from An_{3.6} to An_{29.5}, Ab_{71.9} to Ab_{95.0}, and Or₀ to Or_{1.5}, respectively. The majority of these compositions are Oligoclase (Ab_{71.9–75.0}) and Albite (Ab_{92.0–95.0}) (Fig. 5a) (Deer 1992). This characteristic is compatible with fractional crystallization, playing a pivotal role in influencing the evolving magma composition in the chamber.

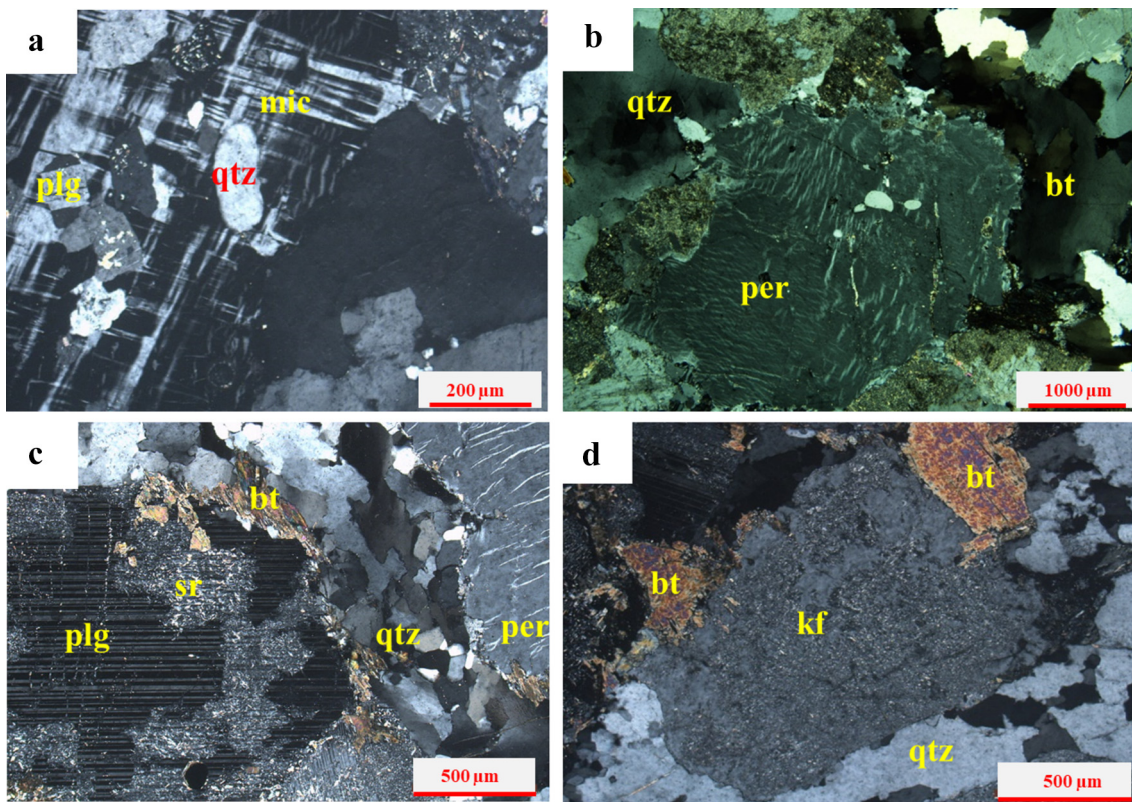


Fig. 3 **a** Microcline exhibiting crosshatched twining with quartz and plagioclase crystals in Armoor granite. **b** coarse-grained perthite hosted quartz crystals and was surrounded by undulose quartz. **c** Plagioclase feldspar display twining associated seritization and recrystallized quartz crystals. **d** Alkali feldspar and biotite are altered to sericite and chlorite and are surrounded by quartz and feldspar minerals

5.1.2 Biotites

The composition of biotites of the studied granite is shown in Table 3, and formulae were determined on an anhydrous base of 22 oxygen per atom. The sum of the primary and reequilibrated biotite analysis's major oxides ranges from 96.1 to 97.7 wt% and 91.75 to 95 wt%, respectively, indicating a variable amount of halogen and OH ions occupancy in the biotite structure. Based on the mineral chemistry of biotites, the Armoor biotites are divided into two types such primary biotites and reequilibrated biotites. The primary and reequilibrated biotites display compositions with $\text{FeO} = 20.5\text{--}22.4$ and $16.74\text{--}19.1$ wt%, $\text{Al}_2\text{O}_3 = 14.1\text{--}14.7$ and $14.99\text{--}16.19$ wt% and $\text{K}_2\text{O} = 8.4\text{--}9.6$ and $8.77\text{--}9.67$ wt%, respectively. TiO_2 is more abundant in the primary biotites than reequilibrated biotites, with levels ranging from 3.7–3.9 and 1.9–3.12 wt%, respectively. The octahedral coordinated mole fractions Mg^{2+} , Fe^{2+} , and Fe^{3+} in the biotite imply that their type is primary to reequilibrated biotites (Fig. 5b) (Nachit et al. 2005), which the reequilibrated biotites impacted by hydrothermal modification (Wones 1980).

Figure 6a depicts the composition of Armoor biotites in the annite-siderophyllite-phlogopite-eastonite

quadrilateral. In general, I-type biotite has more Si and Fe and less Al^{IV} than S-type biotite; both biotite compositions define a trend for I-type granites (Fig. 6b) (Villaseca et al. 2017). The $\text{FeO}^{\text{t}}/\text{MgO}$ ratio of both biotites in granites fluctuates between 1.40 and 2.0, with a mean value of 1.63. These ratios are comparable to those of Mg-biotites ($\text{FeO}^{\text{t}}/\text{MgO} = 1.69$), which are typically associated with amphibole in calc-alkaline (mostly orogenic but also subduction-related) I-type granitoid complexes (Abdel-rahman 1994). Armoor biotite has a greater $\text{Fe}^{2+}/(\text{Fe}^{2+} + \text{Mg})$ ratio, as well as an iron-enrichment index, with higher SiO_2 concentrations ranging from 35.17 to 37.64 wt%. Abdel-rahman (1994) presents a discrimination diagram based on the major-element structure of biotite in igneous rocks crystallized from three distinct magma types. Armoor biotites' FeO^{t} vs MgO and FeO vs Al_2O_3 components indicate evidence of crystallization in a subduction-related calc-alkaline orogenic magma (Fig. 7a, b).

5.2 Temperature and pressure estimations

A study postulated that the Ti concentration of biotite might be used as a geothermometer for graphitic, peraluminous meta-pelites containing rutile or ilmenite and

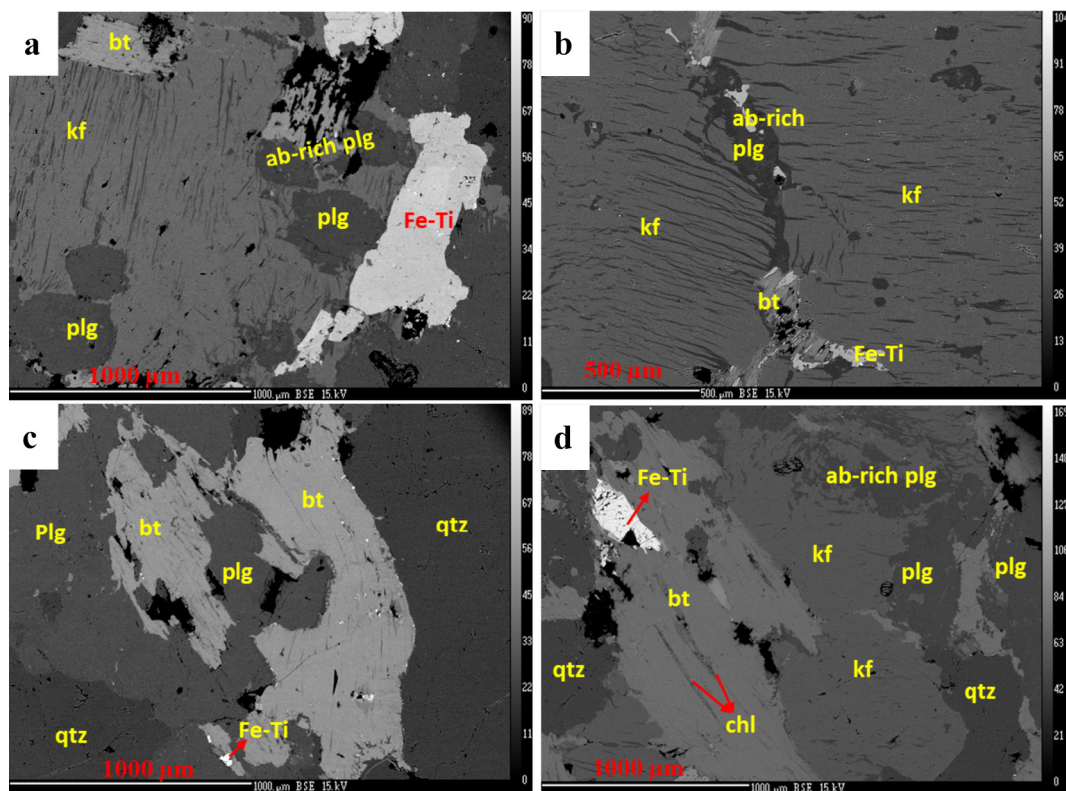


Fig. 4 BSE images of Armoor granites: **a** Large alkali feldspar enclosed plagioclase and albite rich plagioclase with porous nature. **b** Albite-rich patch plagioclase within alkali feldspar associated with biotite. **c** Large biotite crystals hosted plagioclase crystals and small Fe-Ti oxides and were surrounded by quartz. **d** Chlorite flakes and Fe-Ti oxides were observed within biotite surrounded by plagioclase and mixed alkali feldspar and albite-rich plagioclase

equilibrated mately at 4 to 6 kbar (Henry et al. 2005). The proposed method has been applied to granitoid and pegmatitic rocks and appears to produce a reliable exchange temperature estimate (Cesare et al. 2008; Moshefi et al. 2018). Since the majority of biotite grains lie within the specified calibration composition as well as temperature range ($T = 612\text{--}716\text{ }^{\circ}\text{C}$) for this geo-thermometer, the exchange temperature of magmatic biotite was estimated using the previously published equation (Table 3). The primary biotites shows higher temperature ($712\text{--}716\text{ }^{\circ}\text{C}$) than re-equilibrated biotite ($612\text{--}699\text{ }^{\circ}\text{C}$). A research in Japan demonstrated an empirical equation utilizing the total Al concentration of biotite to determine the solidification pressure of barren and fruitful intrusions (Uchida et al. 2007). The primary biotites show lower pressure (1.0–1.4 kbar) than reequilibrated biotite (1.6–2.4 kbar).

5.3 Oxygen fugacity ($f\text{O}_2$)

Usually, the biotite colour in-plane polarized light is commonly used to measure the oxidation level of the magma in which it is formed; the greenish-brown biotite of Armoor granites implies a higher oxidizing environment (Azadbakht et al. 2020). The felsic intrusions of $f\text{O}_2$ may also be

determined with $\text{Fe}^{2+}/(\text{Fe}^{2+} + \text{Mg}^{2+})$ concentration of biotite occurring with K-feldspar and magnetite following the calibration by (Wones and Egster 1965). The $\text{Fe}^{2+}/(\text{Fe}^{2+} + \text{Mg}^{2+})$ vs total Al of Armoor granite display magnetite series with high $f\text{O}_2$ (Fig. 10a) (Anderson et al. 2008), it implies crystalizing under oxidized circumstances. The Armoor biotites solidified at the high oxidizing state (Fig. 10b) of biotite development under NNO buffer, where primary biotites oxygen fugacity ($f\text{O}_2$) = -15.2 to -15.4 (\log_{10} bar); $T = 712\text{--}716\text{ }^{\circ}\text{C}$ and reequilibrated biotites oxygen fugacity ($f\text{O}_2$) = -15.1 to -16.7 (\log_{10} bar); $T = 612\text{--}699\text{ }^{\circ}\text{C}$ (Wones 1972, 1980). These biotites are solidified and developed under the high oxidizing condition of Armoor granites.

5.4 Geochemistry

The Armoor granitic rocks are dominantly composed of silica (71.5–73.5 wt%), CaO (1–1.9 wt%), and minute quantities of MnO, MgO, and TiO₂. The granites include a moderate amount of total alkali (8.7–9.7 wt%) and a moderate to high amount of aluminium (13–13.8 wt%) (Table 4). K₂O concentrations in granites range from 4.8% to 6.4%, whereas Na₂O concentrations range from 3.1% to

Table 1 Calculated values of selected K-feldspar minerals from the Armoor granites

Dataset/Point	AMR-17	AMR-2			NPT-7		
	16 / 1	25 / 1	27 / 1	28 / 1	42 / 1	43 / 1	44 / 1
SiO ₂	63.31	63.04	63.37	62.95	63.94	63.90	63.95
TiO ₂	0.01	0.00	0.00	0.00	0.00	0.02	0.02
Al ₂ O ₃	18.45	18.45	18.50	18.46	18.49	18.68	18.59
Cr ₂ O ₃	0.00	0.00	0.00	0.08	0.01	0.03	0.00
FeO	0.00	0.03	0.03	0.01	0.00	0.00	0.01
MnO	0.00	0.00	0.00	0.01	0.00	0.00	0.00
MgO	0.00	0.02	0.01	0.01	0.01	0.00	0.02
CaO	0.00	0.00	0.00	0.00	0.00	0.00	0.00
Na ₂ O	0.47	0.33	0.49	0.49	0.50	0.65	0.49
K ₂ O	16.13	16.08	15.88	15.91	15.93	15.68	15.88
Total	98.37	97.95	98.28	97.92	98.88	98.96	98.96
<i>Structural formula on the basis of eight oxygen atoms</i>							
Si	2.971	2.974	2.977	2.968	2.987	2.980	2.985
Ti	0.000	0.000	0.000	0.000	0.000	0.001	0.001
Al	1.020	1.026	1.024	1.026	1.018	1.027	1.023
Cr	0.000	0.000	0.000	0.003	0.000	0.001	0.000
Fe ³⁺	0.000	0.001	0.001	0.000	0.000	0.000	0.000
Fe ²⁺	0.000	0.000	0.000	0.000	0.000	0.000	0.000
Mn	0.000	0.000	0.000	0.000	0.000	0.000	0.000
Mg	0.000	0.001	0.001	0.001	0.001	0.000	0.001
Ca	0.000	0.000	0.000	0.000	0.000	0.000	0.000
Ba	0.000	0.000	0.000	0.000	0.000	0.000	0.000
Na	0.043	0.030	0.045	0.045	0.045	0.059	0.044
K	0.966	0.968	0.952	0.957	0.949	0.933	0.946
<i>Mol% of end member</i>							
An	0.00	0.00	0.00	0.00	0.00	0.00	0.00
Ab	4.24	3.02	4.48	4.47	4.55	5.93	4.48
Or	95.76	96.98	95.52	95.53	95.45	94.07	95.52

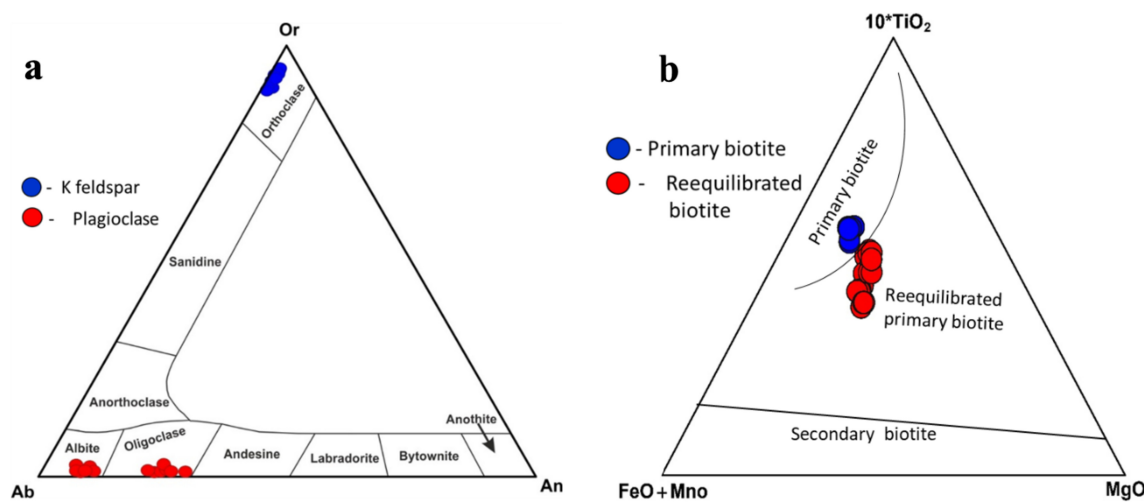
**Fig. 5** **a** Classification diagram of Or-Ab-An for the feldspars from Armoor granitoids (after Deer 1992). **b** Primary and re-equilibrated nature of Armoor biotites as revealed from the $\text{TiO}_2 - \text{FeO} + \text{MnO} - \text{MgO}$ triangular plot (after Nachit et al. 2005)

Table 2 Calculated values of selected Plagioclase minerals from the Armoor granites

Dataset/Point	AMR-17			AMR-2			NPT-7			
	1 / 1	2 / 1	3 / 1	29 / 1	38 / 1	39 / 1	57 / 1	58 / 1	59 / 1	60 / 1
SiO ₂	62.79	61.69	61.86	66.29	61.01	60.69	67.09	66.69	67.59	66.28
TiO ₂	0.00	0.00	0.00	0.01	0.00	0.05	0.00	0.00	0.00	0.00
Al ₂ O ₃	23.65	24.58	24.58	20.18	24.45	24.91	21.01	20.44	21.45	20.84
Cr ₂ O ₃	0.00	0.00	0.05	0.00	0.00	0.00	0.03	0.00	0.00	0.00
FeO	0.01	0.07	0.16	0.05	0.09	0.04	0.06	0.08	0.00	0.03
MnO	0.00	0.00	0.05	0.02	0.05	0.00	0.00	0.00	0.03	0.04
MgO	0.00	0.00	0.00	0.01	0.01	0.00	0.02	0.00	0.01	0.04
CaO	5.18	5.62	5.71	0.78	5.51	6.28	1.50	1.09	1.63	1.28
Na ₂ O	8.79	8.58	8.30	10.99	8.57	8.24	10.88	11.14	10.87	10.97
K ₂ O	0.10	0.11	0.12	0.25	0.28	0.07	0.03	0.05	0.07	0.00
Total	100.62	100.65	100.82	98.56	100.02	100.27	100.62	99.57	101.64	99.46
<i>Structural formula on the basis of eight oxygen atoms</i>										
Si	2.769	2.717	2.728	2.944	2.704	2.688	2.925	2.933	2.918	2.918
Ti	0.000	0.000	0.000	0.000	0.000	0.001	0.000	0.000	0.000	0.000
Al	1.229	1.276	1.277	1.056	1.277	1.300	1.080	1.060	1.091	1.081
Cr	0.000	0.000	0.002	0.000	0.000	0.000	0.001	0.000	0.000	0.000
Fe ³⁺	0.000	0.003	0.000	0.002	0.003	0.001	0.000	0.003	0.000	0.001
Fe ²⁺	0.000	0.000	0.006	0.000	0.000	0.000	0.002	0.000	0.000	0.000
Mn	0.000	0.000	0.002	0.001	0.002	0.000	0.000	0.000	0.001	0.001
Mg	0.000	0.000	0.000	0.001	0.000	0.000	0.001	0.000	0.001	0.003
Ca	0.245	0.265	0.270	0.037	0.262	0.298	0.070	0.051	0.075	0.060
Ba	0.000	0.000	0.000	0.000	0.000	0.000	0.000	0.000	0.000	0.000
Na	0.752	0.733	0.709	0.946	0.736	0.707	0.920	0.950	0.910	0.936
K	0.005	0.006	0.007	0.014	0.016	0.004	0.002	0.003	0.004	0.000
<i>mol% of end member</i>										
An	24.42	26.40	27.35	3.70	25.82	29.53	7.08	5.12	7.63	6.05
Ab	75.05	72.96	71.98	94.91	72.63	70.10	92.76	94.62	92.01	93.95
Or	0.54	0.63	0.67	1.39	1.55	0.38	0.16	0.25	0.36	0.00

4.2%. Pink granites have lower concentrations of Fe₂O₃, MgO, CaO, Na₂O, and TiO₂ than grey granites and higher concentrations of SiO₂ and K₂O than grey granites (Table 4). A connection between three variables Ab–Or–An illustrates an excellent classification of granitoids based on the mineral compositions of sequence with solid solutions, the majority of which are found in the granite field (Barker 1979) (Fig. 8a). These granites range in composition from metaluminous to peraluminous (Fig. 8b) (Frost et al. 2001). The granites have a low Fe[#] (Fig. 8c), indicating that the Armoor samples are magnetic in nature (Frost et al. 2001). These granites have a higher MALI (Modified alkaline lime index), suggesting a typical alkali-calcium composition for continental arc rocks (Fig. 8d). Large ion lithophile elements (LILE), such as Ba, Rb, and Sr, are more prevalent in granite samples than high field strength elements (HFSE) with a higher Sr/Y ratio (Table 5). Chondrite-normalized REE patterns (Nakamura

1974) demonstrate low to high fractionation of LREE/HREE [(La/Yb)_N = 7–132] and moderate fractionation of LREE/MREE [(La/Sm)_N = 1.6–15.8] in Armoor granites (Fig. 9a). In the Normalized primitive mantle diagram, granites have strong positive Rb, Th, U, K, and Pb anomalies and significant negative Ba, Nb, P and Ti anomalies, which indicate to the vital role of crust and subduction zone setting (Fig. 9b) (Sun and McDonough 1989).

6 Discussion

6.1 Mineralogical implications

Biotite's chemical composition might be used to investigate the physicochemical components of its parent magma, such as temperature, pressure, and oxygen fugacity (Wones

Table 3 Calculated values of selected Biotite minerals from the Armor granites

Sample no	Primary biotite						Reequilibrated biotite					
	AMR-17	AMR-17	AMR-17	AMR-17	AMR-17	AMR-17	AMR-2	AMR-2	AMR-2	AMR-2	AMR-2	AMR-2
Sample	13 / 1	15/ 1	17 / 1	27 / 1	28 / 1	31 / 1	34 / 1	36 / 1	37 / 1	40 / 1	41 / 1	42 / 1
SiO ₂	36.47	36.55	35.47	35.67	36.49	35.45	36.66	37.55	37.34	37.64	36.13	35.97
Al ₂ O ₃	14.14	14.12	14.44	14.33	14.35	14.78	16.12	16.04	15.75	16.16	15.79	15.87
Na ₂ O	0.08	0.12	0.08	0.15	0.16	0.14	0.03	0.09	0.13	0.06	0.12	0.04
K ₂ O	9.25	9.12	9.84	8.47	9.65	8.44	9.35	9.17	9.36	9.5	9.21	8.83
MgO	11.55	11.61	11.22	11.31	10.92	11.44	11.64	11.53	11.52	11.32	11.42	10.84
CaO	0.04	0.08	0.04	0.25	0.06	0.04	0	0.23	0.04	0.12	0.11	0.83
TiO ₂	3.79	3.89	3.93	3.79	3.86	3.93	2.66	2.76	3.08	2.8	2.58	2.86
Cr ₂ O ₃	0	0	0	0.06	0	0.05	0	0	0	0.03	0	0
MnO	0.25	0.29	0.31	0.32	0.36	0.27	0.25	0.26	0.3	0.17	0.18	0.09
NiO	0	0	0	0	0	0	0	0.07	0.1	0	0	0.02
FeO	20.53	21.71	22.35	21.95	21.85	22.44	17.66	17.24	17.42	17.64	17.23	17.72
Total	96.1	97.49	97.68	96.3	97.7	96.98	94.38	94.94	95.06	95.43	93.64	93.2
FeO + MgO	32.08	33.32	33.57	33.26	32.77	33.88	29.31	28.77	28.95	28.96	28.64	28.58
FeO/FeO + MgO	0.64	0.65	0.67	0.66	0.67	0.66	0.6	0.6	0.6	0.61	0.62	0.61
FeO + MnO	20.78	22	22.66	22.27	22.21	22.71	17.91	17.5	17.72	17.81	17.41	17.82
10TiO ₂	37.9	38.9	39.3	37.9	38.6	39.3	26.63	27.62	30.82	28.02	25.79	28.63
MgO + MnO	11.8	11.9	11.53	11.63	11.28	11.71	11.894	11.789	11.825	11.49	11.593	10.93
<i>Structural formula on the basis of 22 oxygen atoms</i>												
Si	5.48	5.41	5.29	5.34	5.44	5.25	5.54	5.63	5.65	5.59	5.59	5.42
Fe ³⁺	0.25	0.32	0.40	0.35	0.26	0.43	0.13	0.00	0.02	0.00	0.05	0.20
Fe ²⁺	2.36	2.41	2.44	2.45	2.50	2.41	2.12	2.17	2.18	2.22	2.15	2.30
Ti	0.43	0.44	0.45	0.43	0.44	0.45	0.30	0.31	0.35	0.32	0.30	0.35
Mn	0.03	0.04	0.04	0.04	0.05	0.03	0.03	0.03	0.04	0.02	0.02	0.03
Mg	2.62	2.60	2.54	2.57	2.46	2.58	2.64	2.59	2.54	2.60	2.51	2.64
Ca	0.01	0.01	0.04	0.01	0.01	0.01	0.00	0.04	0.01	0.02	0.14	0.03
Na	0.02	0.03	0.02	0.04	0.05	0.04	0.01	0.03	0.04	0.02	0.02	0.03
K	1.79	1.75	1.91	1.65	1.86	1.63	1.81	1.76	1.80	1.82	1.75	1.74
Σ Al	2.53	2.50	2.59	2.57	2.55	2.63	2.89	2.85	2.80	2.86	2.91	2.88
Xan	0.41	0.42	0.43	0.44	0.42	0.44	0.38	0.39	0.40	0.38	0.41	0.39
Mg/(Fe + Mg)	0.50	0.49	0.47	0.48	0.47	0.48	0.54	0.54	0.53	0.54	0.52	0.53
Fe + Mg	4.97	5.01	4.99	5.02	4.95	4.98	4.75	4.76	4.77	4.75	4.81	4.77
Fe/Fe + Mg	0.47	0.48	0.49	0.49	0.50	0.48	0.45	0.46	0.47	0.45	0.48	0.45
Fe ²⁺ + Mn	2.39	2.44	2.48	2.49	2.54	2.44	2.15	2.21	2.22	2.17	2.31	2.16
Al + Fe ³⁺ + Ti	3.22	3.27	3.44	3.35	3.26	3.51	3.32	3.17	3.18	3.26	3.22	3.47

Table 3 continued

Sample no	Primary biotite						Reequilibrated biotite					
	AMR-17	AMR-17	AMR-17	AMR-17	AMR-17	AMR-17	AMR-2	AMR-2	AMR-2	AMR-2	AMR-2	AMR-2
P(Kbar)	1.1	1.1	1.3	1.3	1.2	1.4	2.2	2.1	1.9	2.1	2.2	2.1
T(°C)	716	716	716	713	713	716	672	677	693	677	668	682
log fO ₂	-15.26	-15.31	-15.32	-15.39	-15.46	-15.28	-15.63	-15.38	-15.69	-15.74	-15.69	-15.39
△FMQ	1.23	1.19	1.14	1.17	1.11	1.17	1.90	1.77	1.60	1.72	1.88	1.56
△NNO	0.53	0.49	0.45	0.48	0.41	0.49	1.24	1.11	0.94	1.06	1.23	0.91
△HM	-4.63	-4.67	-4.70	-4.68	-4.75	-4.65	-3.89	-4.03	-4.20	-4.08	-3.91	-4.22
Sample no	Reequilibrated biotite						AMR-65C	AMR-65C	AMR-54	AMR-54	AMR-54	AMR-54
Sample	98 / 1	99 / 1	14 / 1	15 / 1	16 / 1	17 / 1	27 / 1	28 / 1	1 / 1	3 / 1	4 / 1	10 / 1
SiO ₂	36.88	36.25	36.18	36.95	37.05	37.18	36.51	36.92	37.07	36.41	37.5	36.85
Al ₂ O ₃	15.57	15.45	15.36	15.73	15.78	15.31	15.5	15.47	15.29	15.08	15.38	14.99
Na ₂ O	0.09	0.04	0.1	0.05	0.02	0.11	0.01	0.05	0.1	0.14	0.07	0.09
K ₂ O	9.67	9.5	9.14	9.66	9.52	9.07	9.57	9.62	8.88	8.86	9.56	9.46
MgO	11.19	11.17	10.88	11.3	11.07	11.06	11.52	11.57	11.77	11.9	11.89	12.19
CaO	0	0.01	0.03	0	0.05	0	0	0.02	0.03	0.1	0	0.04
TiO ₂	2.23	2.51	2.12	2.23	2.14	2.19	1.86	1.93	2.7	2.57	2.49	3.12
Cr ₂ O ₃	0	0	0	0.04	0	0.06	0	0	0	0	0.08	0.02
MnO	0.52	0.47	0.15	0.33	0.24	0.43	0.14	0.38	0.19	0.09	0.17	0.23
NiO	0.1	0	0	0	0	0.11	0.01	0	0	0.05	0	0.02
FeO	17.41	17.64	17.8	19.1	18.18	18.78	18.1	17.57	17.15	17.69	16.75	17.7
Total	93.65	93.03	91.75	95.39	94.06	94.3	93.22	93.51	93.18	92.9	93.81	94.71
FeO + MgO	28.6	28.8	28.68	30.4	29.25	29.84	29.62	29.14	28.92	29.59	28.63	29.89
FeO/FeO + MgO	0.61	0.61	0.62	0.63	0.62	0.63	0.61	0.6	0.59	0.6	0.58	0.59
FeO + MnO	17.93	18.11	17.95	19.43	18.42	19.21	18.24	17.95	17.34	17.78	16.92	17.93
10TiO ₂	22.31	25.08	21.16	22.26	21.41	21.93	18.63	19.27	27.03	25.72	24.91	31.23
MgO + MnO	11.708	11.633	11.027	11.625	11.31	11.489	11.657	11.945	11.953	11.993	12.06	12.411
<i>Structural formula on the basis of 22 oxygen atoms</i>												
Si	5.66	5.59	5.65	5.57	5.65	5.60	5.65	5.65	5.58	5.71	5.57	5.65
Fe ³⁺	0.08	0.12	0.09	0.20	0.08	0.13	0.19	0.14	0.06	0.16	0.03	0.06
Fe ²⁺	2.16	2.17	2.24	2.23	2.24	2.27	2.15	2.12	2.13	2.13	2.10	2.12
Ti	0.26	0.29	0.25	0.25	0.25	0.25	0.22	0.22	0.31	0.30	0.29	0.36
Mn	0.07	0.06	0.02	0.04	0.03	0.06	0.02	0.05	0.02	0.01	0.02	0.03
Mg	2.57	2.58	2.54	2.56	2.53	2.52	2.66	2.66	2.68	2.74	2.70	2.76

Table 3 continued

Sample no	Reequilibrated biotite									
	AMR-65C	AMR-65C	AMR-54	AMR-54	AMR-54	AMR-54	AMR-54	AMR-31	AMR-31	AMR-31
Ca	0.00	0.00	0.01	0.00	0.01	0.00	0.00	0.02	0.00	0.01
Na	0.03	0.01	0.03	0.02	0.01	0.03	0.02	0.04	0.02	0.01
K	1.90	1.88	1.83	1.87	1.86	1.77	1.89	1.73	1.75	1.84
$\sum \text{Al}$	2.83	2.82	2.84	2.82	2.85	2.76	2.83	2.76	2.75	2.76
Xan	0.39	0.39	0.40	0.39	0.40	0.40	0.38	0.38	0.38	0.38
Mg/(Fe + Mg)	0.53	0.53	0.52	0.51	0.52	0.51	0.53	0.54	0.55	0.55
Fe + Mg	4.74	4.75	4.79	4.79	4.77	4.79	4.81	4.78	4.87	4.80
Fe/Fe + Mg	0.46	0.46	0.47	0.47	0.47	0.47	0.45	0.44	0.44	0.44
Fe ²⁺ + Mn	2.23	2.23	2.26	2.27	2.28	2.33	2.17	2.17	2.14	2.12
Al + Fe ³⁺ + Ti	3.16	3.23	3.18	3.27	3.18	3.15	3.24	3.17	3.13	3.20
P(Kbar)	2.0	2.0	2.0	2.0	2.0	1.8	2.0	1.9	1.8	1.6
T(°C)	644	664	635	636	633	635	612	620	678	670
log fO ₂	-16.17	-15.84	-16.43	-16.37	-16.47	-16.46	-16.72	-16.55	-15.57	-15.72
△FMQ	2.19	1.95	2.20	2.22	2.23	2.21	2.62	2.56	1.85	1.96
△NNO	1.49	1.28	1.51	1.53	1.53	1.50	1.91	1.84	1.17	1.27
△HM	-3.67	-3.88	-3.66	-3.65	-3.64	-3.68	-3.28	-3.34	-3.98	-3.89

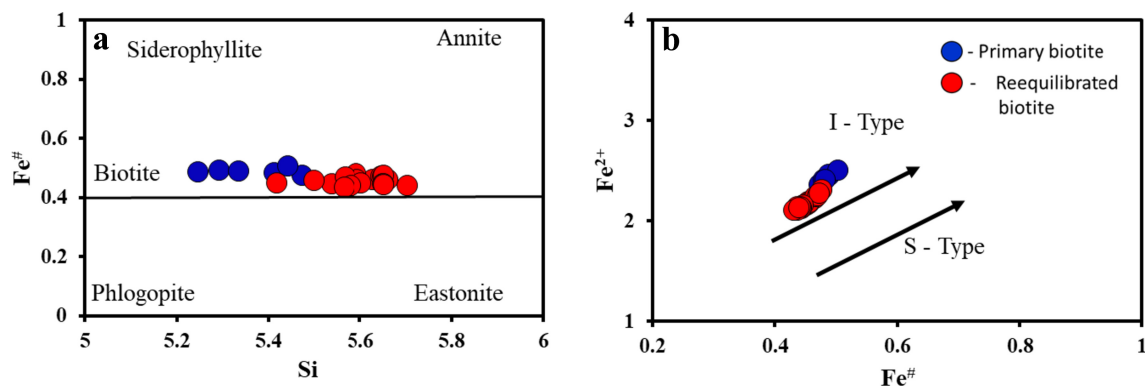


Fig. 6 **a** Composition of biotite from Armoor granite rocks plotted in the annite–siderophyllite–phlogopite–eastonite quadrilateral. **b** Armoor granite biotites define an I-type granite trend in the $\text{Fe}^{\#}$ vs. Fe^{2+} classification diagram (Villaseca et al. 2017)

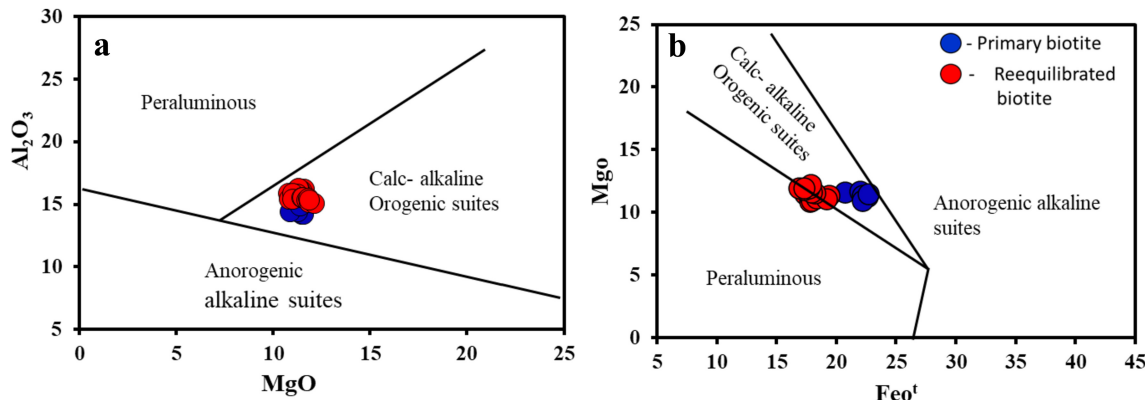


Fig. 7 **a** Al_2O_3 vs MgO , **b** MgO vs Fe^{ot} plots discriminate the host granitoid melt types formed in subduction related calc-alkaline Orogenic suites (after Abdel-Rahman 1994)

Table 4 Major oxides (wt%) of Armoor granites from the northern part of Eastern Dharwar Craton, Telangana

Sample	Grey granites				Pink granites					
	AMR-59	AMR-60	AMR-62	BKD-3	AMR-16	AMR-20	AMR-44	AMR-54	AMR-38	NPT-7
SiO_2	71.69	71.71	71.63	71.55	73.43	73.59	72.99	72.96	73.16	73.5
Al_2O_3	13.63	13.87	13.53	13.47	13.68	13.08	13.71	13.65	13.77	13.26
Fe_2O_3	1.47	1.32	1.29	1.39	0.94	1.07	1.13	1.17	1.22	1.09
MnO	0.01	0.09	0.06	0.06	0.01	0.01	0.02	0.02	0.01	0.01
MgO	0.58	0.52	0.54	0.55	0.31	0.39	0.31	0.32	0.35	0.34
CaO	1.91	1.68	1.61	1.53	1.03	1.01	1.02	1.09	1.08	1.05
Na_2O	4.25	4	3.94	3.97	3.23	3.25	3.16	3.21	3.11	3.35
K_2O	4.87	4.91	4.85	4.96	6.47	6.34	6.49	6.47	6.23	6.39
TiO_2	0.11	0.39	0.39	0.56	0.09	0.18	0.3	0.17	0.11	0.14
P_2O_5	0.05	0.22	0.37	0.63	0.07	0.13	0.08	0.07	0.05	0.06
Total	98.56	98.81	98.4	98.94	99.26	99.05	99.22	99.13	99.08	99.18
Mg#	43.73	43.8	45.16	43.81	39.08	42.2	35.49	35.45	35.98	38.26
$\text{Na}_2\text{O}/\text{K}_2\text{O}$	0.87	0.81	0.81	0.8	0.5	0.51	0.49	0.5	0.5	0.52

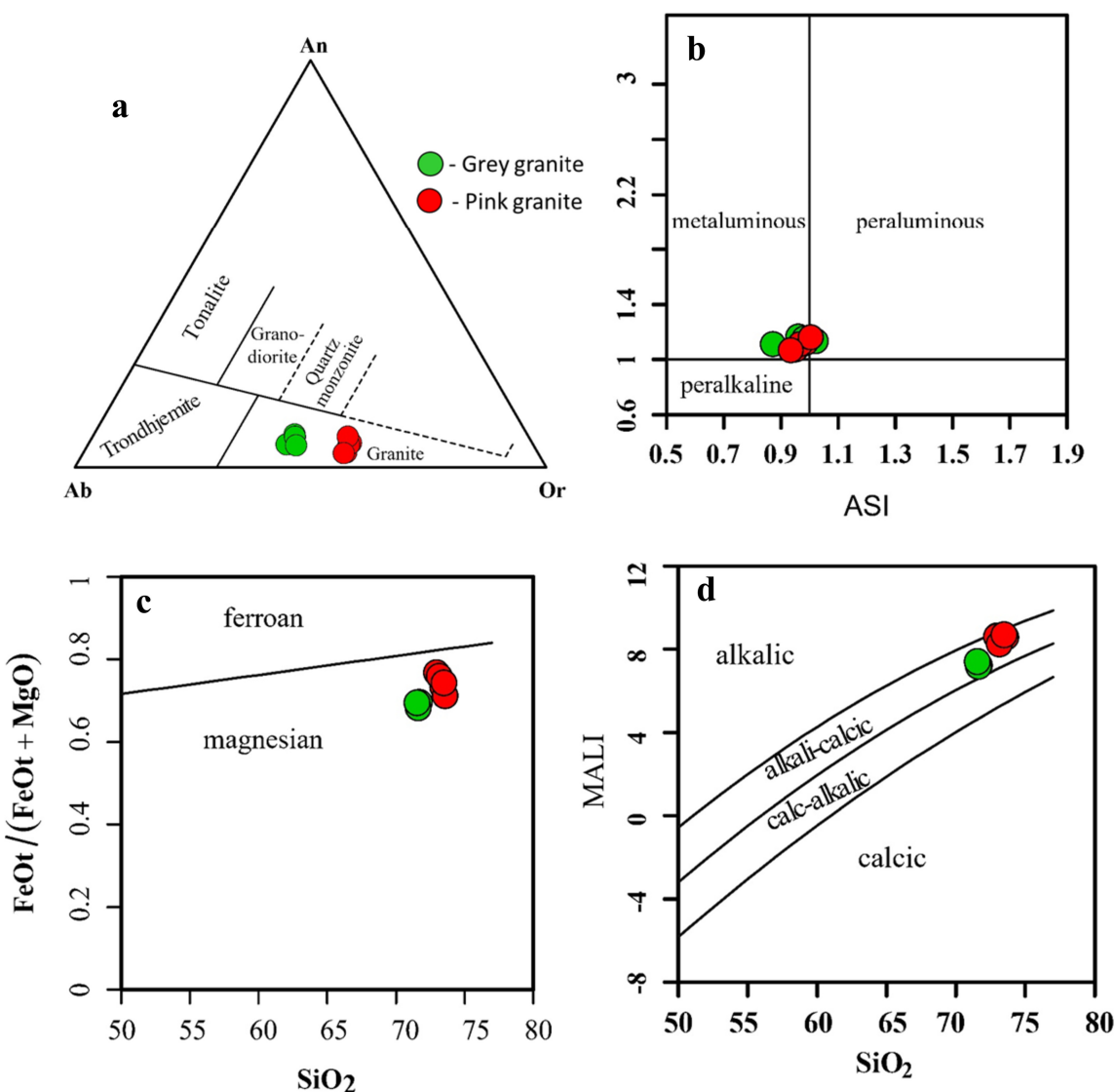


Fig. 8 **a** Ternary diagram An–Ab–Or displaying granite field (O’Conner 1965). **b** Armoor granite shows a metaluminous to peraluminous nature in a diagram based on the (Frost et al. 2001). **c** Fe# vs SiO₂ shows the investigated rocks scatter in the ferroan and magnesian granite fields (Frost et al. 2001). **d** SiO₂ vs MALI (Modified alkaline lime index) diagram indicates the alkali-calcic character of Armoor granites (Frost et al. 2001)

and Eguster 1965; Henry et al. 2005; Uchida et al. 2007; Babazadeh et al. 2019; Azadbakht et al. 2020; Khosravi et al. 2021). Moreover, the biotite color represents the estimated oxygen fugacity of the granite magma, with greenish-brown biotite (Al and Ti-poor and Mg, Fe³⁺ enriched) suggesting that granite magma is oxidized (Lalonde and Bernard 1993; Azadbakht et al. 2020). In addition, the reddish-brown colour of biotite in Sn–W-related intrusions implies magma crystallized reduced conditions (Azadbakht et al. 2020).

Based on petrographic observations (textural correlations) and estimated P–T conditions, it is difficult to determine whether biotite crystallized before or after hornblende in these rocks. Magnesium-rich biotite is frequently found in the same rocks as Fe–Ti oxides, and

simultaneous growth indicates an oxygen fugacity (*f*O₂) in the melt that is rather high (Wones and Eguster 1965). The Fe³⁺/Fe²⁺ ratio in the melt increases as the oxygen fugacity of magmatic systems increases, allowing less Fe²⁺ to compete with Mg²⁺ for site occupancy in mafic minerals. Consequently, when *f*O₂ rises, the Mg[#] of mafic minerals will increase, and it seems that high Mg[#] in mafic minerals is indicative of magmas with a high *f*O₂ content. Utilizing the calibration curves of (Wones and Eguster 1965; Wones 1980) in *f*O₂ – T space, oxygen fugacity values may be analyzed from the Fe²⁺/(Fe²⁺ + Mg²⁺) ratio of the biotite.

The assemblage of titanite + magnetite + quartz in granitoid rocks enables the estimation of relative oxygen fugacity (Wones 1989). When magnetite is present in a

Table 5 Trace and REE compositions (ppm) of Armoor granites from the northern part of Eastern Dharwar Craton, Telangana

Sample	Grey granites				Pink granites					
	AMR-59	AMR-60	AMR-62	BKD-3	AMR-16	AMR-20	AMR-44	AMR-54	AMR-38	NPT-7
Sc	0.91	13.61	9.66	13.42	1.08	2.62	1.7	1.8	1.04	1.92
V	18.89	83.43	68.93	91.2	12.14	28.43	11.84	13.86	16.53	11.02
Cr	147.9	153.33	117.31	160.41	117.49	117.1	124.91	135.96	136.35	126.13
Co	3.16	15.02	13.64	17.58	2.81	6.23	2.79	2.87	3.89	3.33
Ni	5.08	7.67	6.47	12.38	4.97	5.92	5.06	5.79	5.91	6
Cu	1.84	2.24	3.3	4.42	1.39	1.2	1.28	1.25	2.1	3.02
Zn	31.23	76.41	68.65	67.43	34.74	36.59	50.36	36.59	33.13	64.63
Ga	14.92	18.88	19.38	19.32	15.54	16.6	14.88	13.98	14.78	14.72
Rb	147.51	145.65	144.15	155.2	199.16	188.63	150.61	182.7	172.47	181.02
Sr	367.2	355.86	444.33	413.61	160.96	294.87	165.06	153.26	261.43	132.63
Y	7.36	14.83	17.4	18.5	4	5.41	7.44	6.98	5.99	7.9
Zr	219.15	197.63	262.66	483.69	151.8	343.85	197.62	212.37	209.53	199.48
Nb	3.83	12.89	13.11	11.23	5.26	3.77	11.59	11.06	8.24	8.56
Cs	0.92	1.75	0.89	1.58	1.72	0.89	1.19	1.71	1.29	0.97
Ba	1065.09	713.99	1005.43	1116.47	699.7	1151.28	527.21	631.89	786.96	556.61
La	44.29	36.18	73.95	113.95	21.98	113.82	24.15	17.97	65.24	45.97
Ce	84.92	95.97	162.81	234.66	42.06	221.18	46.16	36.98	125.4	102.91
Pr	8.29	14.63	20.05	26.11	4.09	22.18	4.48	4.21	11.46	11.6
Nd	21.61	57.13	64.81	84.78	11.85	62.77	14.44	13.9	23.4	34.24
Sm	2.32	13.83	10.89	15.15	1.74	7.09	2.76	2.93	2.53	5.93
Eu	0.91	1.61	2.01	2.63	1.08	1.76	0.92	0.8	0.94	0.91
Gd	1.11	8.94	6.27	9.12	1.03	3	1.74	1.7	1.69	2.62
Tb	0.14	1.62	1.03	1.5	0.16	0.3	0.27	0.27	0.3	0.44
Dy	0.56	7.69	4.69	6.53	0.67	0.95	1.26	1.05	0.93	1.31
Ho	0.12	1.52	0.93	1.25	0.14	0.18	0.26	0.26	0.19	0.28
Er	0.34	3.99	2.45	3.18	0.42	0.48	0.73	0.67	0.42	0.74
Tm	0.05	0.55	0.34	0.42	0.07	0.07	0.11	0.08	0.06	0.13
Yb	0.38	3.45	2.31	2.71	0.46	0.57	0.79	0.6	0.53	0.75
Lu	0.08	0.49	0.37	0.4	0.08	0.13	0.15	0.13	0.09	0.13
Hf	5.82	5.22	6.22	11.32	4.36	9.2	6.12	6.21	6.52	6.33
Ta	0.52	1.73	0.65	0.69	0.72	0.21	1.69	1.03	0.63	0.63
Pb	37.11	30.43	27.37	37.74	40.88	45.42	50.79	41.38	40.57	44.82
Th	61.16	47.59	15.25	50.2	34.02	94.65	39.16	30.58	60.02	39.96
U	14.3	9.98	2.03	6.12	24.23	5.26	39.44	45.95	5.68	56.87
Sr/Y	109.34	23.99	25.54	22.36	40.27	54.49	22.19	21.96	43.65	16.8
Zr/Hf	37.65	37.86	42.23	42.73	34.82	37.38	32.29	34.20	32.14	31.51
Th/U	4.28	4.77	7.51	8.20	1.40	17.99	0.99	0.67	10.57	0.70
Eu/Eu*	1.75	0.44	0.75	0.69	2.49	1.18	1.29	1.1	1.39	0.71
(La/Yb) _N	78.04	7	21.32	28.03	31.74	132.49	20.27	20	81.72	40.71
(La/Sm) _N	11.73	1.61	4.18	4.63	7.76	9.88	5.39	3.77	15.85	4.77
(Dy/Yb) _N	0.95	1.43	1.3	1.54	0.92	1.07	1.01	1.12	1.12	1.12
SumREE	165.13	247.6	352.93	502.38	85.83	434.48	98.2	81.54	233.18	207.97

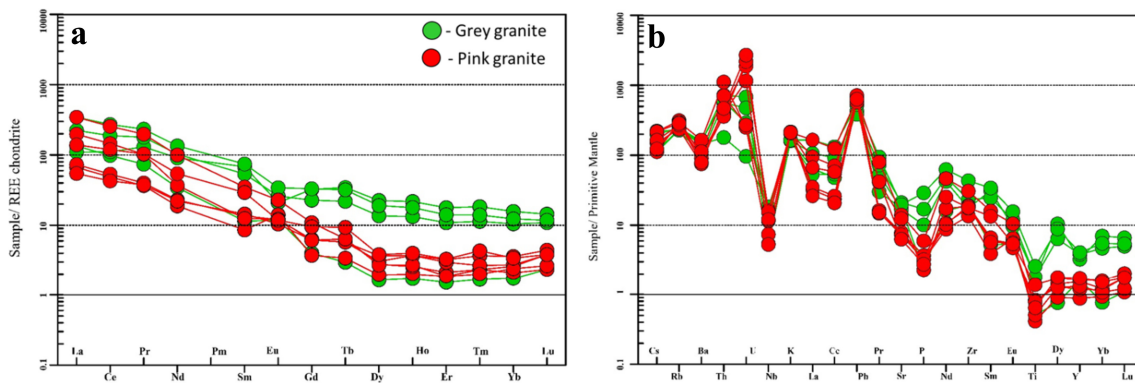


Fig. 9 **a** Chondrite normalized REE patterns of Armoor granites exhibit LREE enrichment and HREE depletion (Nakamura 1974). **b** Primitive mantle normalized trace element distribution pattern of Armoor granite (Sun and McDonough 1989)

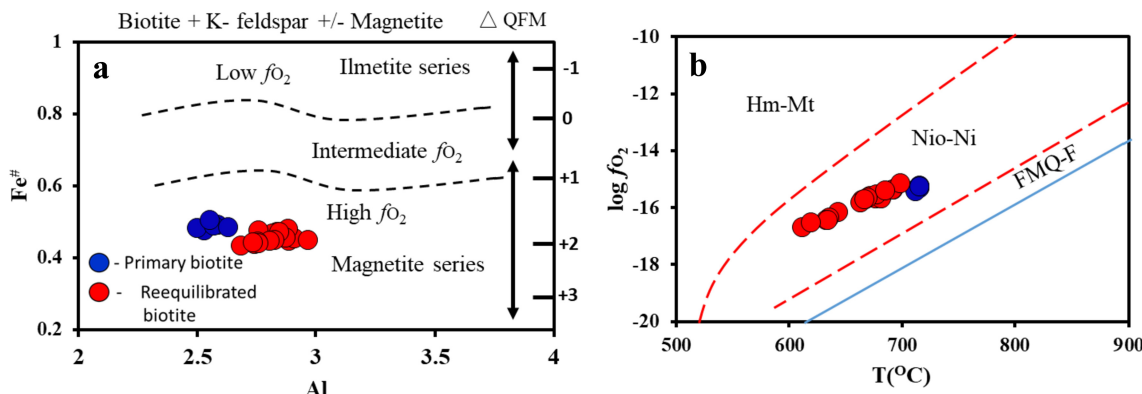


Fig. 10 **a** Binary Al vs Fe# [Fe²⁺/Fe²⁺ + Mg²⁺] plot (apfu) for biotites showing high *fO*₂ and magnetite series (Anderson et al. 2008). **b** Log *fO*₂-T diagram based in biotite chemistry (Wones 1972, 1980), illustrating the redox conditions of Armor biotites

granitic rock assemblage, it is widely accepted that I-type granites are more oxidized than S-type granites (Chappell and White 1992; Helmy et al. 2004; dos Santos Dias et al. 2019). The calculated *fO*₂ values for the Armoor samples fall within a restricted range of oxygen fugacity (*fO*₂) = −15.1 to −16.7(log₁₀ bar), i.e., in the Ni–NiO (NNO) buffers. The majority of biotite compositions in Armoor granitic rocks exhibit Fe[#] values between 0.43 to 0.50, resulting in FQM values between +1.1 to +2.6 (Fig. 10a). Our observations suggest that the Armoor samples crystallized under relatively high *fO*₂ conditions. Wones and Egster (1965), introduced the log *fO*₂-T plot to calculate the balanced biotite + sanidine + magnetite magmatic oxygen fugacity. T-*fO*₂ calculations for the Armoor granitoids equilibrated at oxygen fugacity's between −5.1 to −16.7 indicate crystallization conditions in Ni–NiO (NNO) buffer for all the examined samples, suggesting a relatively high oxidation condition during magma crystallization (Fig. 10b). Magmas originating from the upper mantle have a lower oxygen fugacity FQM (−4 to +3) than magmas derived from the crust (FQM = −2 to +5) (McCammon 2005; Nebel et al.

2015; Babazadeh et al. 2019). The relatively high Oxygen fugacity(*fO*₂) (FQM = 1.1 to 2.6) of Armoor samples allows for much greater crustal contributions.

6.2 Geochemical implications

The Neoarchean granitic activity marks the Archean–Proterozoic boundary in the Dharwar Craton, a crucial event in the processes of crustal formation and remelting (Jayananda et al. 2013). Numerous factors influence the Neoarchean granitoids of EDC, including source structure, melting depth and degree, separation or fractional crystallization, magma mixing, crustal accumulation, and fluid activity (Moyen et al. 2003; Smithies et al. 2003; Martin et al. 2009; Moyen and Martin 2012; Laurent et al. 2014). The present study examines the K-rich Armoor granites of EDC, which exhibits a distinct composition of plagioclase, as well as variance in Ba, Sr, Rb, and Zr concentrations, as well as Zr/Hf, (Eu/Eu*), and LREE ratios, all of which represent crystal accumulation and hydrothermal alteration. Based on the above geochemical characteristics of pink and grey granite of Armoor granites affected by plagioclase

accumulation and hydrothermal alteration, a detailed description is given in the following sentences.

As a result of the early separation of magnetite and amphibole (garnet) and the suppression of plagioclase fractionation in high pH_2O and $f\text{O}_2$ settings, chronically high Sr/Y ratios (16–109) and calc-alkaline tendencies are seen (Zimmer et al. 2010). Several investigations have shown that garnet and amphibole, relics of their parent rocks, display significant Sr/Y and La/Yb dissolution (Lieu and Stern 2019; Nandy et al. 2019). Amphibole, which has a partition coefficient K_d for MREE that is greater than one, consolidates MREE more than HREE, whereas garnet consolidates HREE more than MREE (Davidson et al. 2007; Khosravi et al. 2019). Garnet-rich residues would have a larger Dy/Yb (0.92–1.54) ratio during melting than amphibole-rich residues. These results indicate that the no influence of amphibole residue in Armoor granites and the high Sr/Y ratio suggest that plagioclase accumulation (Macpherson et al. 2006; Davidson et al. 2007; Khosravi et al. 2019; Nagamma et al. 2023). Additionally, petrographic evidence of accumulation, such as large euhedral crystals, dark mafic inclusions feldspar phenocrysts, and recrystallization of plagioclase and K-feldspar (Fig. 2c,d). A clear study on feldspar accumulation with the help of mineralogical and experimental limitations as they indicates widespread and regular recrystallization of the host granites and granodiorites (Glazner and Johnson 2013). In both plutonic (Lowery Claiborne et al. 2006) and volcanic (Reid et al. 2011) processes, the results of zircon fractionation (lowered Zr/Hf ratio) and aggregation (increased Zr/Hf ratio) have been reported. Additionally, the Eu anomaly (Eu/Eu^*) and Sr concentrations help to understand the crystal accumulation in the granitic rocks. The higher Ba, Sr, and Zr/Hf (31.5–42.7) ratio and Eu/Eu^* (0.14–2.4) ratio are present in Armoor granite which is the most promising indicator of crystal accumulation. The Eu anomalies can be used to clarify the function of feldspar in source melting, thus helping understand the magma emplacement process (Tata et al. 2018; Khosravi et al. 2019).

It has been shown that mineral fractionation modifies the Eu's chemical behavior. As a consequence of plagioclase fractionation during magma formation, these granites display strong positive Eu anomalies ($\text{Eu}/\text{Eu}^* = 1.1$ to 2.4) (Macpherson et al. 2006; Davidson et al. 2007). Positive Eu deviations in granitoids may be linked to plagioclase consumption as a source accumulation in the magma chamber (Macpherson et al. 2006; Davidson et al. 2007). There was no substantial association between the Na_2O , CaO , and Sr components and the Eu deviations in any of the group samples considered in the study, which influence of plagioclase accumulation (Fig. 11 a, b, and c) (Zhou et al. 2016). High Sr/Y intermediate-silicic igneous rocks are typically attributable to fractional

crystallization of Y-rich minerals (garnet or amphibole) (Macpherson et al. 2006; Khosravi et al. 2019), or melting of a high Sr/Y source (Kamei et al. 2009). In addition, Wang et al. (2013) proposed that the high Sr/Y leucosomes in the North Dabie Terrane were produced by plagioclase accumulation. Laurent et al. (2020) recommended that the high Sr/Y characteristics of TTGs may be the result of crystal-melt separation dominated by plagioclase accumulation. These investigations suggest that high Sr/Y ratios in silicic igneous rocks could result from crystal-melt separation driven by plagioclase accumulation. The Armoor granites have positive europium anomalies with a greater ratio of Sr/Y (Fig. 11d), and $(\text{Dy}/\text{Yb})_N$ (subscript N represents Chondrite normalized value (Nakamura 1974)), these characteristics all indicate a higher melting pressure of high Sr/Y TTG and a metasediment source with garnet residue.

Hydrothermal alteration is a set of chemical reactions that aims to bring hydrothermal fluids and rocks into chemical equilibrium. These processes affect the mineralogy, chemical composition, and textural properties of granitoids (Tata et al. 2018). Fracture-controlled and less often occurring widespread modifications such as feldspathic, sericitic, silicic, and calc-silicate are common in these rocks. The Armor samples were the following primary alteration forms based on their mineralogy: K-feldspar alteration and sericitization with late carbonate and chlorite overprints (Fig. 3c and d). The rocks within the K-feldspar interstices show varying degrees of alteration and plagioclase relics. Sericitized granitoid samples have a low Na_2O content due to substituting sericite for plagioclase. The HFSC (Nb and Ta) exhibit no positive correlation with Zr (Fig. 12), suggesting that these elements have been mobilized as a result of the alteration (Li and Wei 2017). The fluid fractionation phase is most likely responsible for the Rb enrichment in the Armoor samples with low Ba/Rb, K/Rb, and Nb/Ta ratios (Dostal and Chatterjee 2010; Shellnutt and Dostal 2012). Hydrothermal alteration methods have been discovered to impact on Eu anomaly chemical behavior (Bau 1991; Lottermoser 1992; Tata et al. 2018). The Chondrite normalized values of grey granite (expect AMR-59) show higher TREE (247.6–502.38) and low Eu/Eu^* (0.44–0.75), whereas grey granite (expect NPT-7) shows low TREE (81.54–434.48) and higher Eu/Eu^* (1.1–2.49) (Nakamura 1974). The Chondrite normalized diagram shows dominantly negative Eu anomalies and enrichment of LREE of grey granites and dominantly positive Eu anomalies and depletion of LREE of pink granites, which indicate hydrothermal alteration dominantly influences the grey granites than pink granites (Fig. 9a) (Nakamura 1974).

As indicated by the Th/U (0.6–10) and Zr/Hf (31.5–42.7) ratios, the aluminum saturation index of the

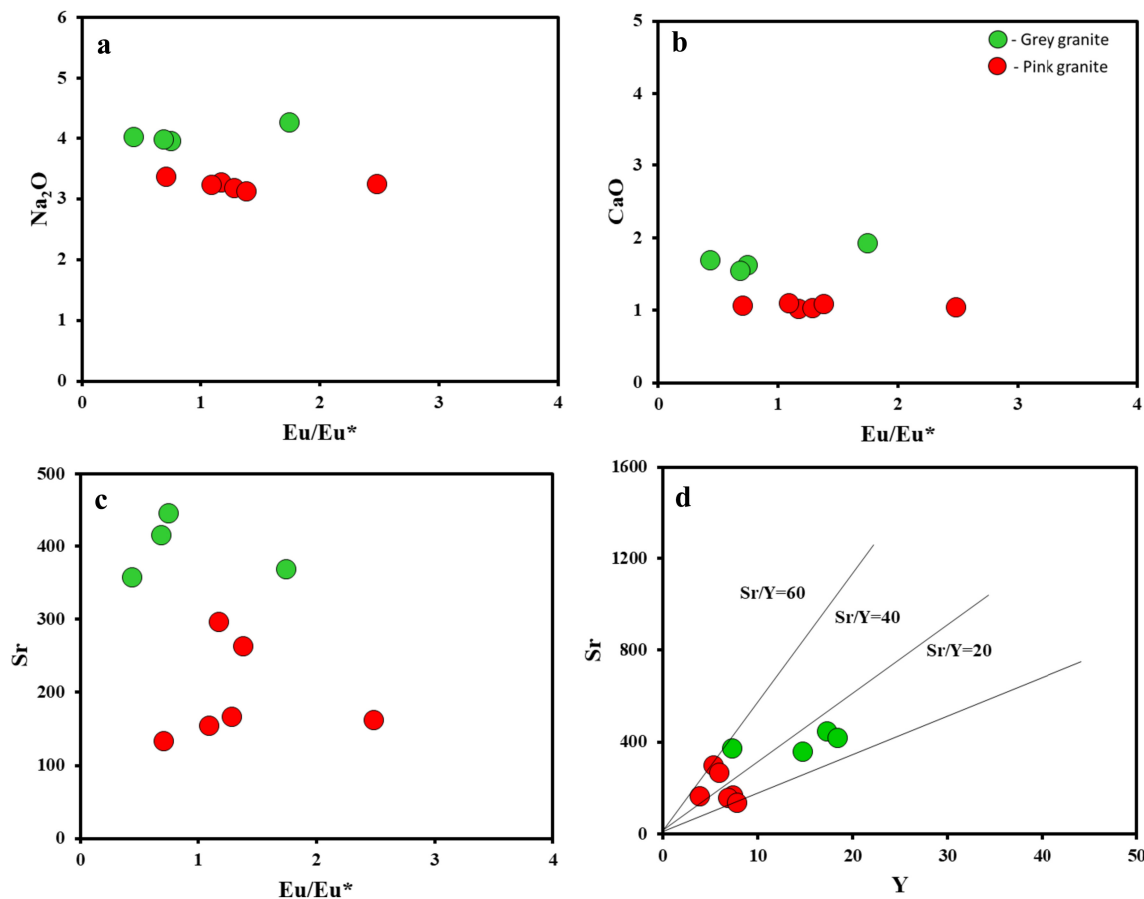


Fig. 11 The variation of selected major and trace elements vs Eu/Eu^* for Armoor granite explain crystal accumulation behavior: **a** Eu/Eu^* vs Na_2O ; **b** Eu/Eu^* vs CaO ; **c** Eu/Eu^* vs Sr ; **d** Y vs Sr plot, Eu/Eu^* normalized value represents REE Chondrite by Nakamura (1974), for Armoor granites (Zhou et al. 2016)

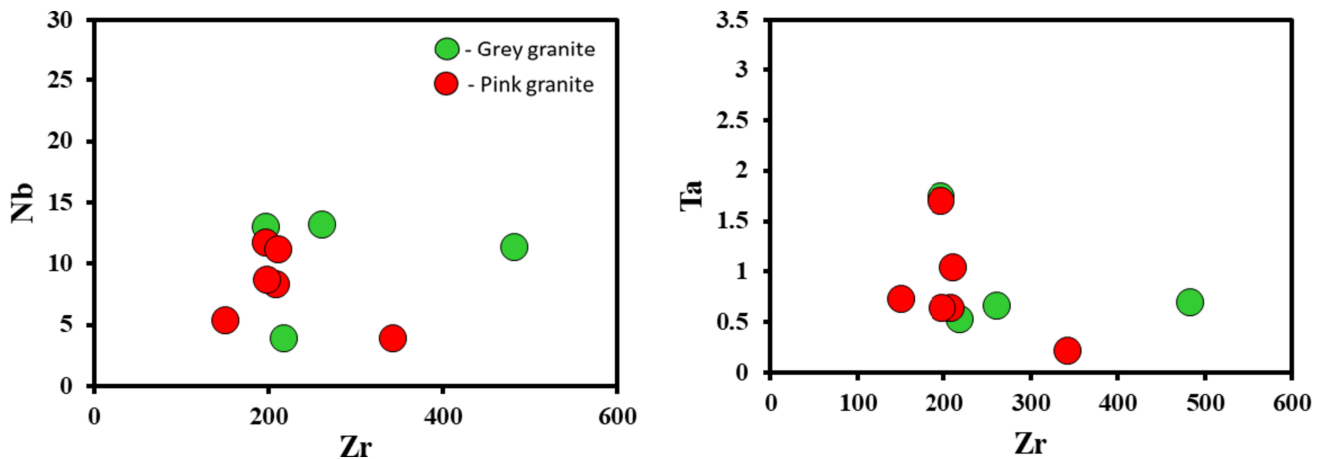


Fig. 12 Zr vs Nb , Ta elements not showing clear positive correlation suggests post-magmatic alteration (Li and Wei 2017)

meta-aluminous to the per-aluminous composition of Armoor granites indicates that these rocks produced through partial melting of continental crustal rocks (Kaya-gusuz et al. 2016). Granites are positioned inside the remelting of the arc crust field on a source discrimination

diagram (Fig. 13a), indicating that they are derived from earlier crustal rocks. As a result, the ternary diagram $(3\text{CaO}-\text{Al}_2\text{O}_3)/(\text{FeO}^\text{t} + \text{MgO}) - 5 \times (\text{K}_2\text{O}/\text{Na}_2\text{O})$ (Fig. 13b) shows that the Armoor granites are produced by TTG and metasedimentary rocks (Laurent et al. 2014). Previous

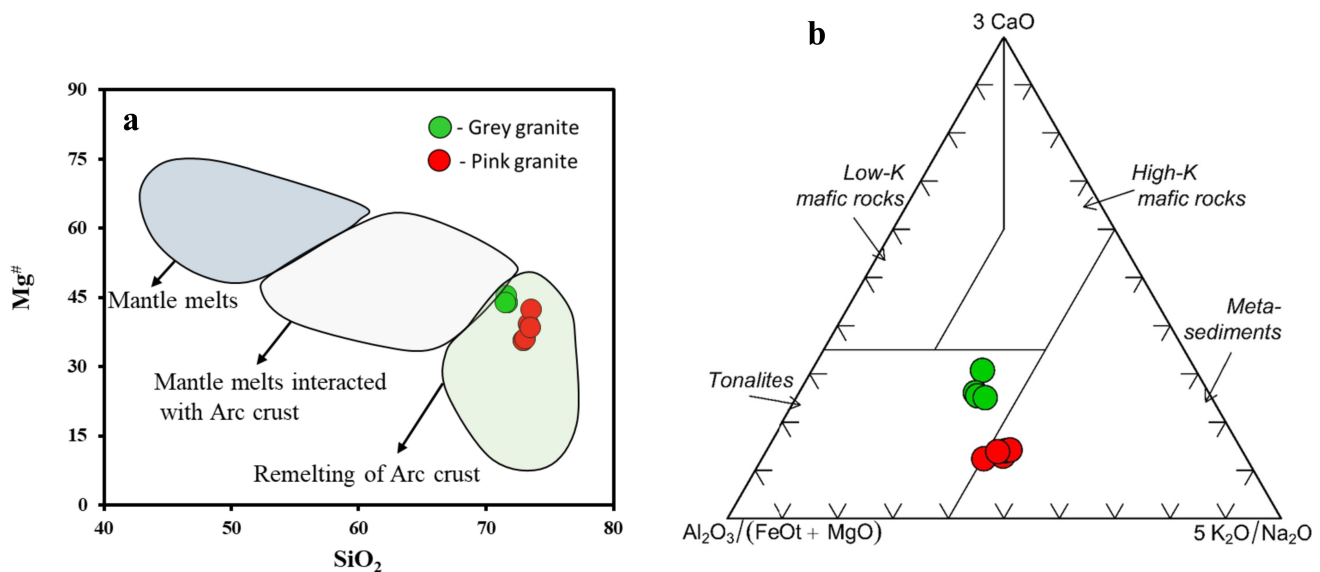
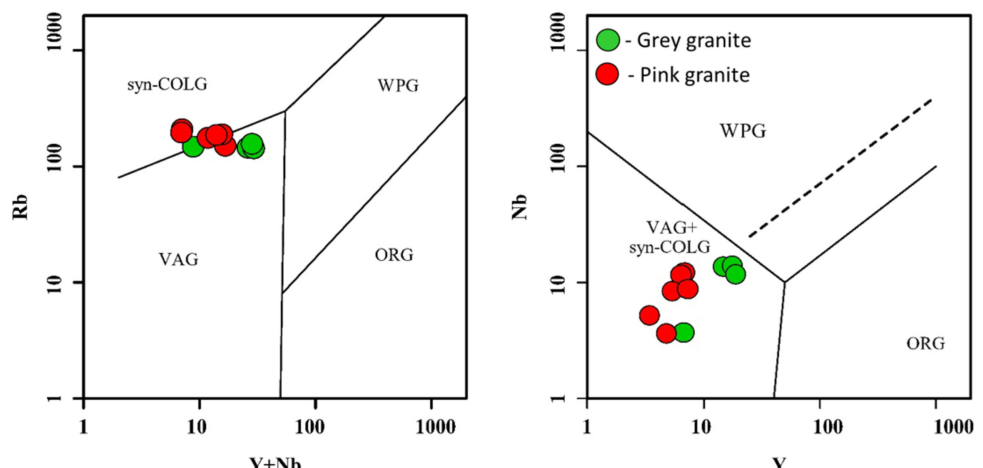


Fig. 13 **a** Source discrimination diagram (with parameters SiO₂ vs Mg#) the Armoor granite falls in the Crustal source (Jayananda et al. 2018). **b** 3CaO-Al₂O₃/(FeOt + MgO)-5×(K₂O/Na₂O) triangular plot (Laurent et al. 2014) depicting the sources of TTGs, and Metasediments

Fig. 14 Armoor granites fall in syn-collisional and volcanic arc settings of the Tectonic discrimination diagram (Pearce et al. 1984). VAG-Volcanic granites, Syn-COLG- Syn collision granites, WPG- Within plate granites, ORG- Ocean ridge granites



experimental studies suggested that Neoarchean granites made up of K-rich biotite granites were found in almost all Archean cratons that had been clarified by the melting of older TTG's and metasediments (Sylvester 1994; Moyen et al. 2003; Laurent et al. 2014; Jayananda et al. 2019; Mohan et al. 2019; Ajay Kumar et al. 2022; Ranga et al. 2022).

The majority of scientists have advocated the geodynamic two-stage growth model (Fig. 11) for Neoarchean granites (Laurent et al. 2014; Dey et al. 2017; Mohan et al. 2019), which is also relevant to the study area. During the transition from subduction to collision, the Neoarchean TTG of the EDC was formed, which represents the stage of phase 1 granitoids. These TTG were formed as a result of the melting of a subducting slab and its interaction with the preexisting crust. In phase 2, following the collision of

the eastern and western cratonic blocks, the sanukitoid, K-rich, and hybrid granitoids variants were formed. In collisional environments, terrane accretion due to continent-continent collision resulting in crustal thickening, followed by slab breakoff or lithospheric delamination, may provide the necessary heat source. The thermal anomaly therefore produced by the collision would trigger partial melting and interactions between crust and mantle components, leading to the occurrence of sanukitoid, K-rich, and hybrid granites (Mikkola et al. 2012; Moyen et al. 2017).

Geochemical properties of Armoor granites prohibit their formation in the volcanic arc and collision conditions, which evolved during the late Archean time in EDC (Frost et al. 2001; Clemens et al. 2010). Negative Ba, Sr, Nb, and Ti anomalies on the primitive mantle normalized trace

element distribution pattern of indicate a subduction zone setting (Fig. 9b) (Sun and McDonough 1989). In addition, the HFSE systematics of these granites suggest that they are syn-collisional and of volcanic arc type in the setting of subduction (Fig. 14) (Pearce et al. 1984; Laurent et al. 2014; Mohan et al. 2019). Based on the previous workers and this work, K-rich Armoor granites formed by subduction to collision environment in the late Archean time, followed by remelting of older TTG and metasedimentary rocks.

7 Conclusions

The biotite mineral chemistry of examined granite implies their provenance-generating metaluminous (I-type) magnetite series (oxidized) granites in a calc-alkaline subduction tectonic context. The Armoor granite displays magnetite series with high Oxygen fugacity (δO_2), which implies crystalizing under oxidized circumstances. The Armoor biotites solidified at the high oxidizing state of biotite development under the NNO buffer. Geochemically, the Armoor granites exhibit higher LREE over HREE, rich (Dy/Yb) and Sr/Y ratios, and negative and positive europium anomalies suggest that they are influenced by plagioclase accumulation and hydrothermal alteration. The Armoor granites show negative Ti, Sr, Ti, and Nb anomalies and high Sr/Y, which suggests the high-pressure melting of source material with garnet residue in a subduction setting. The current study demonstrates that the Armoor granites are generated by remelting older crustal sources.

Acknowledgements The authors thank the Head of the Department of Geology, Osmania University (Hyderabad), for petrography facilities. This work forms a part of the Ph.D. thesis of the first author. We acknowledge to Prof. M. Srinivas, Department of Geology, Osmania University, for his suggestions in the discussion part. Ak thanks the UGC (New Delhi), for awarding RGNF-Research Fellowship. We also thank Narahari, Senior Scientist, GSI- Hyderabad, for help with EPMA analysis. Dr. M. Ram Mohan, Chief Scientist and Dr. Keshava Krishna, Principal Scientist CSIR-NGRI, Hyderabad, for their help with ICP-MS and XRF analysis. The authors are grateful to the anonymous reviewers and handling editor for their constructive suggestions and comments which significantly improved this manuscript.

Declarations

Conflict of interest The authors declare that they have no conflict of interest.

References

- Abdel-rahman AFM (1994) Nature of biotites from alkaline, calc-alkaline, and peraluminous magmas. *J Petrol* 35:525–541. <https://doi.org/10.1093/petrology/35.2.525>
- Ajay Kumar A, Srinivas M, Ch Ashok R, Ranga SA (2022) Geochemistry of K-rich granites from Armoor, Nizamabad district, Telangana: Implications for metasedimentary source. *J Appl Geochemistry* 24:203–215
- Anderson JL, Smith D (1995) The effects of temperature. *Plast Technol* 80:549–559
- Anderson JL, Barth AP, Wooden JL, Mazdab F (2008) Thermometers and thermobarometers in granitic systems. *Rev Mineral Geochemistry* 69:121–142. <https://doi.org/10.2138/rmg.2008.69.4>
- Anettusungla RV, Kumar S (2018) Redox condition, nature and tectono-magmatic environment of granitoids and granite gneisses from the Karbi Anglong Hills, Northeast India: constraints from magnetic susceptibility and biotite geochemistry. *J Geol Soc India* 91:601–612. <https://doi.org/10.1007/s12594-018-0911-0>
- Ashok C, Santhosh GHNV, Vijaya Kumar T, Nagamma J (2021) Evolution of quartz crystals in the Sircilla granite pluton, Southern India: Insights from a Cathodoluminescence study. *J Indian Geophys Union* 25:57–67
- Ashok C, Babu EVSSK, Dash S, Santhosh GHNV (2022a) Redox condition and mineralogical evidence of the magma mixing origin of the Mafic Microgranular Enclaves (MMEs) from Sircilla Granite Pluton (SGP), Eastern Dharwar Craton (EDC), India. *J Geol Soc India* 98:1237–1243
- Ashok C, Santhosh GHNV, Dash S, Ratnakar J (2022b) Magma mixing and mingling during pluton formation: a case study through field, petrography and crystal size distribution (CSD) studies on Sirsilla Granite Pluton, India. *J Geol Soc India* 98:815–821
- Azadbakht Z, Lentz DR, McFarlane CRM, Whalen JB (2020) Using magmatic biotite chemistry to differentiate barren and mineralized Silurian–Devonian granitoids of New Brunswick, Canada. *Contrib to Mineral Petrol* 175:.. <https://doi.org/10.1007/s00410-020-01703-2>
- Babazadeh S, Furman T, Cottle JM et al (2019) Magma chamber evolution of the Ardestan pluton, Central Iran: evidence from mineral chemistry, zircon composition and crystal size distribution. *Mineral Mag* 83:763–780. <https://doi.org/10.1180/mgm.2019.44>
- Balakrishnan S, Rajamani V, Hanson GN (1999) U-Pb ages for zircon and titanite from the Ramagiri area, southern India: Evidence for accretionary origin of the eastern Dharwar Craton during the late Archean. *J Geol* 107:69–86. <https://doi.org/10.1086/314331>
- Barker F (1979) Trondhjemites: definition, environment and hypotheses of origin. *Dev Pet* 6:1–12
- Barrière M, Cotten J (1979) Contributions to mineralogy and biotites and associated minerals as markers of magmatic fractionation and deuterium equilibration in granites. *Contrib Mineral Petrol* 70(2):183–192
- Bau M (1991) Rare-earth element mobility during hydrothermal and metamorphic fluid-rock interaction and the significance of the oxidation state of europium. *Chem Geol* 93:219–230. [https://doi.org/10.1016/0009-2541\(91\)90115-8](https://doi.org/10.1016/0009-2541(91)90115-8)
- Beswick AE (1973) An experimental study of alkali metal distributions in feldspars and micas. *Geochim Cosmochim Acta* 37:183–208. [https://doi.org/10.1016/0016-7037\(73\)90128-2](https://doi.org/10.1016/0016-7037(73)90128-2)
- Bhaskar-Rao YJ, Vijaya-Kumar T, Sreenivas B, Babu EVSSK (2020) A review of Paleo- to Neoarchean crustal evolution in the Dharwar Craton, southern India and the transition towards a plate tectonic regime. *Episodes* 43:51–68. <https://doi.org/10.18814/epiiugs/2020/020003>
- Bora S, Kumar S (2015) Geochemistry of biotites and host granitoid plutons from the Proterozoic Mahakoshal Belt, central India tectonic zone: Implication for nature and tectonic setting of magmatism. *Int Geol Rev* 57:1686–1706. <https://doi.org/10.1080/00206814.2015.1032372>

- Cesare B, Satish-Kumar M, Cruciani G et al (2008) Mineral chemistry of Ti-rich biotite from pegmatite and metapelitic granulites of the Kerala Khondalite Belt (Southeast India): Petrology and further insight into titanium substitutions. *Am Mineral* 93:327–338. <https://doi.org/10.2138/am.2008.2579>
- Chadwick B, Vasudev VN, Hegde GV (2000) The Dharwar Craton, southern India, interpreted as the result of Late Archaean oblique convergence. *Precambrian Res* 99:91–111. [https://doi.org/10.1016/S0301-9268\(99\)00055-8](https://doi.org/10.1016/S0301-9268(99)00055-8)
- Chappell BW, White AJR (1992) I- and S-type granites in the Lachlan Fold Belt. *Trans R Soc Edinb Earth Sci* 83:1–26. <https://doi.org/10.1017/S0263593300007720>
- Chardon D, Jayananda M, Chetty TRK, Peucat JJ (2008) Precambrian continental strain and shear zone patterns: South Indian case. *J Geophys Res Solid Earth* 113:1–16. <https://doi.org/10.1029/2007JB005299>
- Chardon D, Jayananda M, Peucat JJ (2011) Lateral constrictional flow of hot orogenic crust: Insights from the Neoarchean of south India, geological and geophysical implications for orogenic plateaux. *Geochem Geophys Geosyst*. <https://doi.org/10.1029/2010GC003398>
- Davidson JP, Morgan DJ, Charlier BLA et al (2007) Microsampling and isotopic analysis of igneous rocks: Implications for the study of magmatic systems. *Annu Rev Earth Planet Sci* 35:273–311. <https://doi.org/10.1146/annurev.earth.35.031306.140211>
- Deer WA, Howie RA, Zussman J (1992) An introduction to the rock-forming minerals. Longman Scientific & Technical, Hong Kong
- Dey S, Rai AK, Chaki A (2009) Geochemistry of granitoids of Bilgi area, northern part of eastern Dharwar craton, southern India: example of transitional TTGs derived from depleted source. *J Geol Soc India* 73:854–870. <https://doi.org/10.1007/s12594-009-0068-y>
- Dey S, Pandey UK, Rai AK, Chaki A (2012) Geochemical and Nd isotope constraints on petrogenesis of granitoids from NW part of the Eastern Dharwar Craton: possible implications for late Archaean crustal accretion. *J Asian Earth Sci* 45:40–56. <https://doi.org/10.1016/j.jseas.2011.09.013>
- Dey S, Nandy J, Choudhary AK et al (2015) Neoarchean crustal growth by combined arc-plume action: evidence from the Kadiri Greenstone Belt, eastern Dharwar Craton, India. *Geol Soc Spec Publ* 389:135–163. <https://doi.org/10.1144/SP389.3>
- Dey S, Halla J, Kurhila M et al (2017) Geochronology of Neoarchean granitoids of the NW Eastern Dharwar Craton: Implications for crust formation. *Geol Soc Spec Publ* 449:89–121. <https://doi.org/10.1144/SP449.9>
- Dey S, Pal S, Balakrishnan S et al (2018) Both plume and arc: Origin of Neoarchean crust as recorded in Veligallu greenstone belt, Dharwar craton, India. *Precambrian Res* 314:41–61. <https://doi.org/10.1016/j.precamres.2018.04.019>
- dos Santos Dias JC, Gonçalves L, Gonçalves CC (2019) Contrasting oxygen fugacity of I- and S-type granites from the Araúáí orogen, SE Brazil: an approach based on opaque mineral assemblages. *Mineral Petrof* 113:667–686. <https://doi.org/10.1007/s00710-019-00670-2>
- Dostal J, Chatterjee AK (2010) Lead isotope and trace element composition of K-feldspars from peraluminous granitoids of the Late Devonian South Mountain Batholith (Nova Scotia, Canada): Implications for petrogenesis and tectonic reconstruction. *Contrib Mineral Petrof* 159:563–578. <https://doi.org/10.1007/s00410-009-0442-1>
- Friend CRL, Nutman AP (1991) SHRIMP U-Pb geochronology of the Closepet granite and Peninsular gneiss, Karnataka, south India. *J - Geol Soc India* 38:357–368
- Frost BR, Barnes CG, Collins WJ et al (2001) A geochemical classification for granitic rocks. *J Petrol* 42:2033–2048. <https://doi.org/10.1093/petrology/42.11.2033>
- Gireesh RV, Sekhamo KÜ, Jayananda M (2012) Anatomy of 257–252 Ga granitoid plutons in the eastern Dharwar craton, southern India: implications for magma chamber processes and crustal evolution. *Episodes* 35:398–413. <https://doi.org/10.18814/epiugs/2012/v35i3/002>
- Glazner AF, Johnson BR (2013) Late crystallization of K-feldspar and the paradox of megacrystic granites. *Contrib Mineral Petrof* 166:777–799. <https://doi.org/10.1007/s00410-013-0914-1>
- Helmy HM, Ahmed AF, El Mahallawi MM, Ali SM (2004) Pressure, temperature and oxygen fugacity conditions of calc-alkaline granitoids, Eastern Desert of Egypt, and tectonic implications. *J African Earth Sci* 38:255–268. <https://doi.org/10.1016/j.jafrearsci.2004.01.002>
- Henry DJ, Guidotti CV, Thomson JA (2005) The Ti-saturation surface for low-to-medium pressure metapelitic biotites: Implications for geothermometry and Ti-substitution mechanisms. *Am Mineral* 90:316–328. <https://doi.org/10.2138/am.2005.1498>
- Hokada T, Horie K, Satish-Kumar M et al (2013) An appraisal of Archaean supracrustal sequences in Chitradurga Schist Belt, Western Dharwar Craton, Southern India. *Precambrian Res* 227:99–119. <https://doi.org/10.1016/j.precamres.2012.04.006>
- Jayananda M, Martin H, Peucat JJ, Mahabaleswar B (1995) Late Archaean crust-mantle interactions: geochemistry of LREE-enriched mantle derived magmas. Example of the Closepet batholith, southern India. *Contrib to Mineral Petrof* 119:314–329. <https://doi.org/10.1007/BF00307290>
- Jayananda M, Moyen JF, Martin H et al (2000) Late Archaean (2550–2520 Ma) juvenile magmatism in the Eastern Dharwar craton, southern India: constraints from geochronology, Nd-Sr isotopes and whole rock geochemistry. *Precambrian Res* 99:225–254. [https://doi.org/10.1016/S0301-9268\(99\)00063-7](https://doi.org/10.1016/S0301-9268(99)00063-7)
- Jayananda M, Chardon D, Peucat JJ, Capdevila R (2006) 2.61 Ga potassic granites and crustal reworking in the western Dharwar craton, southern India: tectonic, geochronologic and geochemical constraints. *Precambrian Res* 150:1–26. <https://doi.org/10.1016/j.precamres.2006.05.004>
- Jayananda M, Peucat JJ, Chardon D et al (2013) Neoarchean greenstone volcanism and continental growth, Dharwar craton, southern India: constraints from SIMS U-Pb zircon geochronology and Nd isotopes. *Precambrian Res* 227:55–76. <https://doi.org/10.1016/j.precamres.2012.05.002>
- Jayananda M, Santosh M, Aadhiseshan KR (2018) Formation of Archean (3600–2500 Ma) continental crust in the Dharwar Craton, southern India. *Earth-Science Rev* 181:12–42. <https://doi.org/10.1016/j.earscirev.2018.03.013>
- Jayananda M, Aadhiseshan KR, Kusiak MA et al (2020) Multi-stage crustal growth and Neoarchean geodynamics in the Eastern Dharwar Craton, southern India. *Gondwana Res* 78:228–260. <https://doi.org/10.1016/j.gr.2019.09.005>
- Jayananda M, Guitreau M, Tarun Thomas T, et al (2019) Geochronology and geochemistry of Meso- to Neoarchean magmatic epidote-bearing potassic granites, western Dharwar Craton (Bellur-Nagamangala–Pandavpura corridor), southern India: implications for the successive stages of crustal reworking and cratonization. *Geol Soc London, Spec Publ* SP489–2018–125. <https://doi.org/10.1144/sp489-2018-125>
- Kamei A, Miyake Y, Owada M, Kimura JI (2009) A pseudo adakite derived from partial melting of tonalitic to granodioritic crust, Kyushu, southwest Japan arc. *Lithos* 112:615–625. <https://doi.org/10.1016/j.lithos.2009.05.024>
- Kaygusuz A, Arslan M, Sipahi F, Temizel İ (2016) U-Pb zircon chronology and petrogenesis of Carboniferous plutons in the northern part of the Eastern Pontides, NE Turkey: constraints for Paleozoic magmatism and geodynamic evolution. *Gondwana Res* 39:327–346. <https://doi.org/10.1016/j.gr.2016.01.011>

- Khanna TC, Sesha Sai VV, Bizimis M, Krishna AK (2016) Petrogenesis of ultramafics in the Neoarchean Veligallu greenstone terrane, eastern Dharwar craton, India: constraints from bulk-rock geochemistry and Lu-Hf isotopes. *Precambrian Res* 285:186–201. <https://doi.org/10.1016/j.precamres.2016.09.020>
- Khosravi M, Rajabzadeh MA, Qin KZ, Asadi HH (2019) Tectonic setting and mineralization potential of the Zefreh porphyry Cu-Mo deposit, central Iran: constraints from petrographic and geochemical data. *J Geochem Explor* 199:1–15. <https://doi.org/10.1016/j.gexplo.2019.01.001>
- Khosravi M, Christiansen EH, Rajabzadeh MA (2021) Chemistry of rock-forming silicate and sulfide minerals in the granitoids and volcanic rocks of the Zefreh porphyry Cu-Mo deposit, central Iran: implications for crystallization, alteration, and mineralization potential. *Ore Geol Rev*. <https://doi.org/10.1016/j.oregeorev.2021.104150>
- Kocak K, Zedef V, Kansun G (2011) Magma mixing/mingling in the Eocene Horoz (Nigde) granitoids, Central southern Turkey: Evidence from mafic microgranular enclaves. *Mineral Petrol* 103:149–167. <https://doi.org/10.1007/s00710-011-0165-7>
- Krishna AK, Murthy NN, Govil PK (2007) Multielement analysis of soils by wavelength-dispersive X-ray fluorescence spectrometry. *At Spectrosc* 28:202–214
- Krogstad EJ, Hanson GN, Rajamani V (1995) Sources of continental magmatism adjacent to the Late Archean Kolar Suture Zone, south India: distinct isotopic and elemental signatures of two late Archean magmatic series. *Contrib Mineral Petrol* 122:159–173. <https://doi.org/10.1007/s004100050119>
- Kumar S, Pieru T, Rino V, Hayasaka Y (2017) Geochemistry and U-Pb SHRIMP zircon geochronology of microgranular enclaves and host granitoids from the South Khasi Hills of the Meghalaya Plateau, NE India: evidence of synchronous mafic-felsic magma mixing-fractionation and diffusion in a post, pp 253–289
- Kumar S, Pathak M (2010a) Mineralogy and geochemistry of biotites from proterozoic granitoids of Western Arunachal Himalaya: Evidence of bimodal granitogeny and tectonic affinity. *J Geol Soc India* 75:715–730. <https://doi.org/10.1007/s12594-010-0058-0>
- Kumar S, Pathak M (2010b) Mineralogy and geochemistry of biotites from Proterozoic granitoids of western Arunachal Himalaya: evidence of bimodal granitogeny and tectonic affinity. *J Geol Soc India* 75:715–730. <https://doi.org/10.1007/s12594-010-0058-0>
- Lalonde AE, Bernard P (1993) Composition and color of biotite from granites: two useful properties in the characterization of plutonic suites from the Hepburn internal zone of Wopmay Orogen, Northwest Territories. *Can Mineral* 31:203–217
- Laurent O, Martin H, Moyen JF, Doucelance R (2014) The diversity and evolution of late-Archean granitoids: evidence for the onset of “modern-style” plate tectonics between 3.0 and 2.5 Ga. *Lithos* 205:208–235
- Laurent O, Björnsen J, Wotzlaw JF et al (2020) Earth’s earliest granitoids are crystal-rich magma reservoirs tapped by silicic eruptions. *Nat Geosci* 13:163–169. <https://doi.org/10.1038/s41561-019-0520-6>
- Li Z, Wei C (2017) Two types of Neoarchean basalts from Qingyuan greenstone belt, North China Craton: Petrogenesis and tectonic implications. *Precambrian Res* 292:175–193. <https://doi.org/10.1016/j.precamres.2017.01.014>
- Lieu WK, Stern RJ (2019) The robustness of Sr/Y and La/Yb as proxies for crust thickness in modern arcs. *Geosphere* 15:621–641. <https://doi.org/10.1130/GES01667.1>
- Lottermoser BG (1992) Rare earth elements and hydrothermal ore formation processes. *Ore Geol Rev* 7:25–41. [https://doi.org/10.1016/0169-1368\(92\)90017-F](https://doi.org/10.1016/0169-1368(92)90017-F)
- Lowery Claiborne L, Miller CF, Walker BA et al (2006) Tracking magmatic processes through Zr/Hf ratios in rocks and Hf and Ti zoning in zircons: an example from the Spirit Mountain batholith, Nevada. *Mineral Mag* 70:517–543. <https://doi.org/10.1180/0026461067050348>
- Machev P, Klain L, Hecht L (2004) Mineralogy and chemistry of biotites from the Belogradchik Pluton - some petrological implications for granitoid magmatism in North-west Bulgaria. *Bulg Geol Soc*, pp 16–17
- Macpherson CG, Dreher ST, Thirlwall MF (2006) Adakites without slab melting: high pressure differentiation of island arc magma, Mindanao, the Philippines. *Earth Planet Sci Lett* 243:581–593. <https://doi.org/10.1016/j.epsl.2005.12.034>
- Manikyamba C, Kerrich R (2012) Eastern Dharwar Craton, India: Continental lithosphere growth by accretion of diverse plume and arc terranes. *Geosci Front* 3:225–240. <https://doi.org/10.1016/j.gsf.2011.11.009>
- Manikyamba C, Ganguly S, Santosh M et al (2015) Arc-nascent back-arc signature in metabasalts from the Neoarchaean Jonnagiri greenstone terrane, Eastern Dharwar Craton, India. *Geol J* 50:651–669. <https://doi.org/10.1002/gj.2581>
- Martin H, Moyen JF, Rapp R (2009) The sanukitoid series: magmatism at the Archaean-Proterozoic transition. *Earth Environ Sci Trans R Soc Edinburgh* 100:15–33. <https://doi.org/10.1017/S1755691009016120>
- McCammon C (2005) The paradox of mantle redox. *Science* 308:807–808. <https://doi.org/10.1126/science.1110532>
- Mikkola P, Lauri LS, Käpyaho A (2012) Neoarchean leucogranitoids of the Kianta Complex, Karelian Province, Finland: Source characteristics and processes responsible for the observed heterogeneity. *Precambrian Res* 206–207:72–86. <https://doi.org/10.1016/j.precamres.2012.02.010>
- Mohan MR, Asokan AD, Wilde SA (2019) Crustal growth of the Eastern Dharwar Craton: a Neoarchean collisional orogeny? *Geol Soc London, Spec Publ* SP489-2019-108. <https://doi.org/10.1144/sp489-2019-108>
- Moshefi P, Hosseini-zadeh MR, Moayyed M, Lentz DR (2018) Comparative study of mineral chemistry of four biotite types as geochemical indicators of mineralized and barren intrusions in the Sungun Porphyry Cu-Mo deposit, northwestern Iran. *Ore Geol Rev* 97:1–20. <https://doi.org/10.1016/j.oregeorev.2018.05.003>
- Moyen JF, Martin H (2012) Forty years of TTG research. *Lithos* 148:312–336. <https://doi.org/10.1016/j.lithos.2012.06.010>
- Moyen JF, Martin H, Jayananda M, Auvray B (2003) Late Archaean granites: A typology based on the Dharwar Craton (India). *Precambrian Res* 127:103–123. [https://doi.org/10.1016/S0301-9268\(03\)00183-9](https://doi.org/10.1016/S0301-9268(03)00183-9)
- Moyen JF, Laurent O, Chelle-Michou C et al (2017) Collision vs. subduction-related magmatism: Two contrasting ways of granite formation and implications for crustal growth. *Lithos* 277:154–177. <https://doi.org/10.1016/j.lithos.2016.09.018>
- Nachit H, Ibhi A, Abia EH, Ben Ohoud M (2005) Discrimination entre biotites magmatiques primaires, biotites rééquilibrées et biotites néoformées. *Comptes Rendus Geosci* 337:1415–1420. <https://doi.org/10.1016/j.crte.2005.09.002>
- Nagamma J, Ratnakar J, Ajay-Kumar A, Ashok CH (2023) Geochemical studies of hybrid granite from Madugulapalli area, Eastern Dharwar Craton, Southern India: Implications for crustal mixing. *Acta Geochim* 42:9–23. <https://doi.org/10.1007/s11631-022-00568-5>
- Nagamma J, Ashok C (2022) Microstructural studies on the Madugulapalli Granites, Eastern Dharwar Craton, southern India, vol 26, pp 144–154
- Nakamura N (1974) Determination of REE, Ba, Fe, Mg, Na and K in carbonaceous and ordinary chondrites. *Geochim Cosmochim*

- Acta 38:757–775. [https://doi.org/10.1016/0016-7037\(74\)90149-5](https://doi.org/10.1016/0016-7037(74)90149-5)
- Nandy J, Dey S, Heilimo E (2019) Neoarchaean magmatism through arc and lithosphere melting: evidence from eastern Dharwar Craton. *Geol J* 54:3148–3166. <https://doi.org/10.1002/gj.3498>
- Nebel O, Sossi PA, Bénard A et al (2015) Redox-variability and controls in subduction zones from an iron-isotope perspective. *Earth Planet Sci Lett* 432:142–151. <https://doi.org/10.1016/j.epsl.2015.09.036>
- Nutman AP, McGregor VR, Friend CRL et al (1996) The Itsaq Gneiss Complex of southern West Greenland; the world's most extensive record of early crustal evolution (3900–3600 Ma). *Precambrian Res* 78:1–39. [https://doi.org/10.1016/0301-9268\(95\)00066-6](https://doi.org/10.1016/0301-9268(95)00066-6)
- Pearce JA, Harris NBW, Tindle AG (1984) Trace element discrimination diagrams for the tectonic interpretation of granitic rocks. *J Petrol* 25:956–983. <https://doi.org/10.1093/petrology/25.4.956>
- Peucat JJ, Mahabaleswar B, Jayananda M (1993) Age of younger tonalitic magmatism and granulitic metamorphism in the South Indian transition zone (Krishnagiri area); comparison with older Peninsular gneisses from the Gorur-Hassan area. *J Metamorph Geol* 11:879–888. <https://doi.org/10.1111/j.1525-1314.1993.tb00197.x>
- Prabhakar BC, Jayananda M, Shareef M, Kano T (2009) Petrology and geochemistry of late archaean granitoids in the northern part of Eastern Dharwar Craton, Southern India: implications for transitional geodynamic setting. *J Geol Soc India* 74:299–317. <https://doi.org/10.1007/s12594-009-0137-2>
- Raju BV, Asokan AD, Pandey R et al (2022) Neoarchean crust–mantle interactions from the Eastern Dharwar Craton: insights from mineral chemistry of the Nizamabad granites, southern India. *J Earth Syst Sci.* <https://doi.org/10.1007/s12040-022-01903-3>
- Ranga R, Srinivas M, Ch Ashok J, Ratnakar AA, Kumar MD, KRP, (2022) Geochemistry and petrogenesis of the nawabpet granitoids from Mahabubnagar district, Telangana, Southern India. *J Appl Geochemistry* 24:229–240
- Reid MR, Vazquez JA, Schmitt AK (2011) Zircon-scale insights into the history of a Supervolcano, Bishop Tuff, Long Valley, California, with implications for the Ti-in-zircon geothermometer. *Contrib Mineral Petrol* 161:293–311. <https://doi.org/10.1007/s00410-010-0532-0>
- Ridolfi F, Renzulli A, Puerini M (2010) Stability and chemical equilibrium of amphibole in calc-alkaline magmas: An overview, new thermobarometric formulations and application to subduction-related volcanoes. *Contrib to Mineral Petrol* 160:45–66. <https://doi.org/10.1007/s00410-009-0465-7>
- Sallet R (2000) Fluorine as a tool in the petrogenesis of quartz-bearing magmatic associations: applications of an improved F-OH biotite-apatite thermometer grid. *Lithos* 50:241–253. [https://doi.org/10.1016/S0024-4937\(99\)00036-5](https://doi.org/10.1016/S0024-4937(99)00036-5)
- Shellnutt JG, Dostal J (2012) An evaluation of crustal assimilation within the Late Devonian South Mountain Batholith, SW Nova Scotia. *Geol Mag* 149:353–365. <https://doi.org/10.1017/S0016756811000665>
- Sheykhi M, Rezaei-Kahkhaei M, Ghasemi HA (2019) Biotite and feldspar chemistry: an approach to the petrogenesis of the Gapdan pluton (NW of Zahedan). *Iran J Crystallogr Mineral* 27:635–648. <https://doi.org/10.29252/ijcm.27.3.635>
- Shukla S, Mohan MR (2019) Magma mixing in Neoarchaean granite from Nalgonda region, Eastern Dharwar Craton, India: morphological, mineralogical and geochemical evidences. *J Earth Syst Sci* 128:1–27. <https://doi.org/10.1007/s12040-019-1095-8>
- Singh B, Kumar S (2005) Petrogenetic appraisal of early Palaeozoic granitoids of Kinnaur District, Higher Himalachal Himalaya, India. *Gondwana Res* 8:67–76. [https://doi.org/10.1016/S1342-937X\(05\)70263-X](https://doi.org/10.1016/S1342-937X(05)70263-X)
- Singh B, Kumar S (2008) Geochemistry of biotite, muscovite and tourmaline from Early Palaeozoic granitoids of Kinnaur district, Higher Himalachal Himalaya. *Himal J Sci* 2:248–249. <https://doi.org/10.3126/hjs.v2i4.930>
- Smithies RH, Champion DC, Cassidy KF (2003) Formation of Earth's Early Archaean continental crust. *Precambrian Res* 127:89–101. [https://doi.org/10.1016/S0301-9268\(03\)00182-7](https://doi.org/10.1016/S0301-9268(03)00182-7)
- Speer JA, Solberg TN, Becker SW (1981) Petrography of the uranium-bearing minerals of the Liberty Hill pluton, South Carolina: Phase assemblages and migration of uranium in granitoid rocks. *Econ Geol* 76:2162–2175. <https://doi.org/10.2113/gsecongeo.76.8.2162>
- Sun SJ, Zhang RQ, Cong YN, et al (2020) Analogous diagenetic conditions of dark enclave and its host granite derived by magma mixing: evidence for a post-mixing magmatic process. *Lithos* 356–357
- Sun SS, McDonough WF (1989) Chemical and isotopic systematics of oceanic basalts: implications for mantle composition and processes. *Geol Soc Spec Publ* 42:313–345. <https://doi.org/10.1144/GSL.SP.1989.042.01.19>
- Sylvester PJ (1994) Archean granite plutons. *Dev Precambrian Geol* 11:261–314. [https://doi.org/10.1016/S0166-2635\(08\)70225-1](https://doi.org/10.1016/S0166-2635(08)70225-1)
- Tata E, Suh CE, Vishiti A et al (2018) Wallrock alteration categories and their geochemical signatures in gold-bearing neoproterozoic granitoids, Batouri Gold district, Southeastern Cameroon. *Geochemistry Explor Environ Anal* 19:269–288. <https://doi.org/10.1144/geea2016-017>
- Tischendorf G, Förster H-J, Gottesmann B (2001) Minor- and trace-element composition of trioctahedral micas: a review. *Mineral Mag* 65:249–276. <https://doi.org/10.1180/002646101550244>
- Uchida E, Endo S, Makino M (2007) Relationship between solidification depth of granitic rocks and formation of hydrothermal ore deposits. *Resour Geol* 57:47–56. <https://doi.org/10.1111/j.1751-3928.2006.00004.x>
- Villaseca C, Ruiz-Martínez VC, Pérez-Soba C (2017) Magnetic susceptibility of Variscan granite-types of the Spanish central system and the redox state of magma. *Geol Acta* 15:379–394. <https://doi.org/10.1344/GeologicaActa2017.15.4.8>
- Wang SJ, Li SG, Chen LJ et al (2013) Geochronology and geochemistry of leucosomes in the North Dabie Terrane, East China: implication for post-UHPM crustal melting during exhumation. *Contrib Mineral Petrol* 165:1009–1029. <https://doi.org/10.1007/s00410-012-0845-2>
- Wen G, Li JW, Hofstra AH et al (2017) Hydrothermal reequilibration of igneous magnetite in altered granitic plutons and its implications for magnetite classification schemes: Insights from the Handan-Xingtai iron district, North China Craton. *Geochim Cosmochim Acta* 213:255–270. <https://doi.org/10.1016/j.gca.2017.06.043>
- Wones DR (1972) Stability of biotite: a reply. *Am Mineral J Earth Planet Mater* 57:316–317
- Wones DR (1980) Contributions of crystallography, mineralogy, and petrology to the geology of the Lucerne pluton, Hancock County, Maine. *Am Mineral* 65:411–437
- Wones DR, Eguster HP (1965) Stability of biotite: experiment, theory and application. *Am Mineral* 50:1228–1272
- Yavuz F (2003) Evaluating micas in petrologic and metallogenetic aspect: part II-applications using the computer program Mica+. *Comput Geosci* 29:1215–1228. [https://doi.org/10.1016/S0098-3004\(03\)00143-2](https://doi.org/10.1016/S0098-3004(03)00143-2)
- Yuguchi T, Sasao E, Ishibashi M, Nishiyama T (2015) Hydrothermal chloritization processes from biotite in the Toki granite, Central Japan: temporal variations of of the compositions of

- hydrothermal fluids associated with chloritization. *Am Mineral* 100:1134–1152. <https://doi.org/10.2138/am-2015-5126>
- Zhou XC, Zhang HF, Luo BJ et al (2016) Origin of high Sr/Y-type granitic magmatism in the southwestern of the Alxa Block, Northwest China. *Lithos* 256–257:211–227. <https://doi.org/10.1016/j.lithos.2016.04.021>
- Zhu C, Sverjensky DA (1992) F-Cl-OH partitioning between biotite and apatite. *Geochim Cosmochim Acta* 56:3435–3467. [https://doi.org/10.1016/0016-7037\(92\)90390-5](https://doi.org/10.1016/0016-7037(92)90390-5)
- Zimmer MM, Plank T, Hauri EH et al (2010) The role of water in generating the calc-alkaline trend: New volatile data for aleutian magmas and a new tholeiitic index. *J Petrol* 51:2411–2444. <https://doi.org/10.1093/petrology/egq062>

Springer Nature or its licensor (e.g. a society or other partner) holds exclusive rights to this article under a publishing agreement with the author(s) or other rightsholder(s); author self-archiving of the accepted manuscript version of this article is solely governed by the terms of such publishing agreement and applicable law.